

PFC/JA-87-43

**Experimental Study of the Hot Electron
Plasma Equilibrium
in the Constance B Mirror Experiment**

Xing Chen, B.G. Lane, D.L. Smatlak,
R.S. Post, and S.A. Hokin

October, 1987

Plasma Fusion Center
Massachusetts Institute of Technology
Cambridge, Massachusetts 02139 USA

Submitted to publication in: The Physics of Fluids

Abstract

Constance B mirror is a single cell quadrupole magnetic mirror in which high beta ($\beta \leq 0.3$), hot electron plasmas ($T_e = 400$ keV) are created with up to 4 kW of fundamental electron cyclotron resonance heating (ECRH). Details of the plasma equilibrium profile are quantitatively determined by fitting model plasma pressure profiles to the data from four complementary measurements: diamagnetic loops and magnetic probes, x-ray pinhole cameras, visible light TV cameras, and thermocouple probes. The experimental analysis shows that the equilibrium pressure profile of an ECRH generated plasma in a baseball magnetic mirror is hollow and the plasma is concentrated along a baseball seam shaped curve. The hollowness of the hot electron density profile is 50 ± 10 percent. The baseball seam shaped equilibrium profile coincides with the drift orbit of deeply trapped electrons in the quadrupole mirror field. Particle drift reversal is predicted to occur for the model pressure profile which best fits the experimental data under the typical operating conditions. When the ECRH resonance is just above the magnetic minimum, the plasma pressure closely approaches the mirror mode beta limit.

I. Introduction

Minimum-B magnetic configurations play an unique role in the study of the magnetic mirror confinement. An absolute minimum-B mirror is expected to be stable to all magnetohydrodynamic (MHD) perturbations.¹ Most current tandem mirror configurations rely on minimum-B end cells to provide overall MHD stability.²⁻⁷ In the Constance B mirror experiment, the hot electron plasma properties in a single cell quadrupole minimum-B magnetic field are studied.^{5,8,9}

Hot electron plasmas have been the subject of a number of experiments in the past. High beta electron cyclotron resonant heating (ECRH) generated plasmas were first studied in the ELMO experiment,¹⁰ where hot electron plasmas were created with second harmonic heating. ELMO demonstrated the existence of stable hot electron rings in maximum-B mirrors and the ability to maintain them with relatively low amounts of microwave power. This development led to the concept of the utilization of hot electron plasmas to modify the magnetic field geometry and to provide MHD stability to plasmas confined in a bumpy torus (EBT concept). Detailed hot electron ring equilibrium and stability studies have been conducted in EBT,¹¹ SM-1¹² and other experiments.¹³ Magnetic gradient reversal in axisymmetric mirrors has been reported.¹²

Hot electron plasmas have also been studied in minimum-B magnetic mirrors such as INTEREM.¹⁴ The plasmas were generated with fundamental ECRH in a closed mod-B magnetic well. The plasma profile was observed to be restricted to magnetic field lines on which the ECRH resonance occurred. In the axial direction, the plasma was observed to peak at the magnetic minimum and the axial length contracted with increasing ECRH power. However, the three dimensional plasma equilibrium was not clear.

In this paper, we present an experimental study of the equilibrium properties of the ECRH generated hot electron plasma in the Constance B mirror. The equilibrium is characterized by a hollow plasma profile which concentrates along a baseball seam curve.

The equilibrium profile coincides with the drift orbit of electrons deeply trapped in the quadrupole mirror field. The equilibrium exists in steady state during shots of several seconds, and the plasma diamagnetism decays on a time scale of 2 seconds. In reference 8, we have reported the general structure of this plasma equilibrium. The purpose of this paper is to present the quantitative determination of the equilibrium pressure profile from a set of measurements with diamagnetic loops, an x-ray pinhole camera system, a visible light TV camera system, magnetic probes, skimmer probes, thermocouple probes, and end loss detectors.

The organization of this paper is as follows. Section II describes the experimental setup and the conditions for the equilibrium measurement. Section III presents experimental evidence showing the hollow, baseball seam equilibrium pressure profile. In section IV, we describe some general properties of a mirror confined plasma and give a physical picture of a plasma equilibrium from both single particle motion and fluid theories. The analysis establishes a basis for the plasma pressure models which are used in the equilibrium determination.

Section V presents experimental data measured during the standard operating conditions from four independent measurements, and shows how the equilibrium profiles change under different experimental conditions. The equilibrium pressure profile is quantitatively analyzed by comparing the experimental data with model pressure profiles. Because magnetic measurements have been a primary method in the determination of plasma equilibrium in many experiments, and because we have found certain limitations by using them in Constance, we will give a detailed description of the analysis. In section VI, the results of the experiment are discussed. The magnetic gradient is one of the key elements in the stability analysis. We have calculated the gradient change for the standard shot and found that gradient reversal is achieved. Experimentally, stability of the plasma does not require gradient reversal because the equilibrium is stable at all

values of beta (1 – 50 %). We will also show that the mirror mode limit on plasma beta is closely approached in some experimental conditions. Finally, section VII summarizes the results of the equilibrium experiments.

II. Experimental Arrangement

The magnetic field of the Constance B mirror is produced by a coil shaped like a baseball seam. The plasma confining region is an absolute minimum-B well with quadrupole symmetry. The mirror ratio along the magnetic axis is 1.9. Fig. 1 shows the magnetic field contours and the experimental setup for the equilibrium study. The plasma is created and heated by up to 4 kW of microwave power at 10.5 GHz, which corresponds to a resonant magnetic field of 3.75 kG for nonrelativistic electrons. The resonance occurs on a closed, egg-shaped mod-B surface. The time histories of the plasma density and diamagnetism are shown in Fig. 2.

Plasma conditions in the experiment are usually controlled by the magnetic field strength, the ECRH microwave power, and the ambient neutral gas pressure. Stable plasma equilibria have been generated in a wide parameter regime ($B_0 = 2.2 - 3.75$ kG, ECRH power = 10 W - 4 kW, gas pressure = $2 \times 10^{-7} - 5 \times 10^{-5}$ Torr). Hydrogen is normally used as the working gas but helium, argon and xenon plasmas have also been studied. The standard operating condition in which the equilibrium is measured is $B_0 = 3$ kG, ECRH power = 2 kW, and a hydrogen gas pressure of 5×10^{-7} Torr. The pulse length is 2 seconds. Under the standard operating condition, the plasma reaches steady state in about 0.2-0.3 seconds after the ECRH is turned on and the plasma beta is 30 percent.

The line integrated plasma density is measured with a 24 GHz microwave interferometer located at the midplane. It is oriented at 45 degrees with respect to the horizontal axis. The hot electron and the cold electron densities are determined from the interferometer signal decay. After the ECRH is turned off, the fast drop of density is due to the loss of the electrostatically confined cold electrons ($E \leq 100$ eV), and the subsequent slow decay corresponds to loss of the magnetically confined hot electrons. The interferometer signal from the relativistic electron plasma is multiplied by a factor of $\langle \gamma \rangle$ to compen-

sate for the relativistic mass shift of these electrons. The hot electron and cold electron densities are $3 \times 10^{11} \text{ cm}^{-3}$ and $2 \times 10^{11} \text{ cm}^{-3}$, respectively. The chord averaged hot electron temperature is determined from the bremsstrahlung x-ray radiation spectrum measured with a sodium-iodide scintillation detector located at the midplane. The spatial temperature profile has been measured in an axial scan in the horizontal symmetry plane and a radial scan at $z=3.1 \text{ cm}$. The measurement indicates that the chord averaged hot electron temperature varies from 350 – 400 keV at the peak pressure locations to about 60 keV at the edge. However, in order to invert the chord averaged energy spectra to obtain the radial temperature profile, one has to first unfold the spectra for each energy channel, which results in spectra vs. radius, and then determine the temperature vs. radius from each of the inverted spectra. Because of the limited number of data points and the uncertainties in the target density profile, as well as the complicated magnetic geometry involved, the detailed radial temperature profile has not yet been determined.

An x-ray pinhole camera system and a visible light TV camera system give detailed two dimensional images of the plasma. A Pulnix TM-34K charge-coupled device (CCD) camera is used in the TV camera system. It records the image in a 384×491 array and has a time resolution of 30 ms/frame. The plasma image is displayed on a TV monitor and subsequently stored on tape with a video cassette recorder. The camera can be located either on the midplane or at the end of the machine. The x-ray image of the plasma is measured with the x-ray pinhole camera. The x-rays are imaged by a cone-shaped lead pinhole of 1 mm diameter located on the machine midplane. A $12.7 \mu\text{m}$ thick beryllium foil is used as both the x-ray and vacuum window. The spatial resolution at the center of plasma is 1 cm, which is 1/20 of the plasma diameter. The energy cutoff of the x-ray window is 3 keV. Time integrated x-ray images are recorded by direct exposure of the x-ray film. Fluorescent intensifying screens are also used with x-ray film. These screens select an energy window of 50–200 keV x-ray photons and can reduce the exposure time

by a factor of 3 to 4. This energy response is desirable since the x-ray flux in this range is insensitive to the variation in the plasma temperature profile. However, the spatial resolution is degraded by about a factor of 2 with the use of these screens. The x-ray film is calibrated using the plasma as an x-ray source. The calibration covers an exposure range much wider than that over which the film is normally used, and the film density is measured to be linearly proportional to the x-ray intensity. Time resolved x-ray images are obtained with a scintillation TV camera system. In this system, the x-ray image is converted to visible light by a 2 mm thick CsI(Tl) crystal scintillator. The visible image is then transmitted through a fiber-optic image scope to a microchannel plate (MCP) image intensifier and amplified by a factor of 40,000. The amplified image is subsequently recorded with a CCD TV camera. The time resolution of the system is determined by the speed of the TV camera, which is 30 ms/frame.

The plasma diamagnetic fields are measured by a set of diamagnetic loops and magnetic probes. Three diamagnetic loops with different geometries (circular, elliptical and baseball seam shaped) are installed at three axial locations. The spatial magnetic field distributions outside the plasma are measured with B-dot and Hall probes. These probes are calibrated to within 5 percent accuracy and are sensitive to magnetic field changes of less than 0.1 Gauss. Details of these magnetic probes have been given elsewhere.¹⁵ The ratios of the magnetic signals are independent of plasma beta since each of the signals is proportional to the plasma pressure, and are thus functions of plasma profile only. The ratio between the midplane diamagnetic loop and the magnetic probe signals is the most sensitive to plasma profile changes and is used in the equilibrium study.

Skimmer probes are inserted into the plasma as limiters to determine the radial and axial extent of the hot electrons. Chromel-Alumel thermocouples are used with skimmer probes so that the plasma energy at the probe position can be measured. The thermocouple joint is soldered inside a 3 mm diameter stainless steel shell, and it is

supported only by the two wires to minimize thermal conduction. The reference joint is at the connector end of the probe. Thus room temperature is used as the reference point. The thermocouple calibration is tabulated up to 1370 C° .

III. Baseball Seam Plasma Equilibrium

In this section, we will summarize the experimental evidence to show that the hot electron plasma is confined in a baseball seam curve inside the ECRH resonance surface.

The equilibrium plasma profile can be seen from the x-ray and visible light images of the plasma. Fig. 3a. and 3b. show visible light photographs of the plasma looking perpendicular and parallel to the magnetic axis. These images are taken 60 msec after the ECRH is turned off, when the cold electrons have scattered into the loss cone and only the hot electrons are still confined. X-ray images measured with the x-ray pinhole camera agree with the visible light photographs, and show that the hot electrons are contained in the "C" shaped region. Fig. 3c. shows an x-ray picture obtained with the direct exposure method. The x-ray images measured at different energy ranges are the same. These visible and x-ray photographs show that the hot electron plasma is primarily confined within the ECRH resonant surface and there is a hollow region in its center. Looking along the axis (Fig. 3b.), there are four bright balls on the diagonal chords and a dimmer region near the axis. Looking from the side, it shows a "C" shaped plasma and the opening corresponds to the position where there is longest line-of-sight due to the magnetic flux fanning.

Because of the quadrupole symmetry of the vacuum magnetic field, the plasma image taken from the top of the machine is the same as those taken from the side except that the opening of the "C" is rotated by 180 degrees. A hollow plasma provided in the shape of a baseball seam will produce these images. To confirm this speculation, simulation of chord integrated model plasma profiles are compared with the camera pictures. Fig. 4

shows the line integrations of two model plasma profiles in the Constance magnetic field. With the model profile which peaks on the axis (Fig. 4a.), the image is always peaked since the line-of-sight is longest on the axis. If the plasma is sufficiently hollow (Fig. 4b.), the image will be "C" shaped from the side view and four balls from the end view, as has been observed in the experiment. We will show in the next section that a deeply trapped, hollow plasma profile will naturally form a baseball seam shape in the Constance magnetic field.

This baseball seam plasma profile is also confirmed by skimmer probe measurements. Skimmer probes are inserted into the opening of the "C" to test for hot electrons. Fig. 5 is a plot of the diamagnetic loop signal versus the skimmer probe radial position at $z = -10$ cm. It shows that the total plasma diamagnetism is barely perturbed even though the probe is well inside the ECRH resonance surface, which is nearly 9 cm at this axial location. However, during this scan, the probe is carefully kept on the horizontal symmetry plane. If the probe is 1 cm off the symmetry plane, no hot electrons can be generated.

Fig. 6 shows the end loss power measured with a scintillator probe outside the mirror peak. It shows a hollow end loss profile and implies that the ECRH power is absorbed mostly by the plasma in the baseball seam.

Combining these experimental observations, it is clear that the plasma is confined along a baseball seam curve. In order to quantitatively determine the plasma equilibrium pressure profile, a good pressure model is needed. We will analyze the equilibrium properties of the quadrupole minimum-B mirror to establish the plasma model in the next section. The detailed experimental data analysis will be presented in section 5.

IV. Plasma Modelling

The purpose of this paper is to quantitatively characterize the plasma equilibrium pressure profile in the Constance experiment. The determination is done by comparing the experimental data with the predictions of model plasma profiles. In this section, we will first analyze the plasma equilibrium properties from both single particle motion and MHD theories. Based on this analysis, we will then develop a plasma pressure profile model for the numerical calculation.

A. Equilibrium Relations

Particle drift motion plays an important role in mirror confined plasma equilibria where the plasma confinement time is long compared with the particle drift time. The equilibrium properties of such a plasma, therefore, should be understandable from both single particle motion and fluid theories.

It is well known that in the limit that the particle Larmor radius is small compared with characteristic magnetic scale lengths, the drift motion of a mirror confined particle is characterized by three adiabatic invariants, the total energy ϵ , the magnetic moment μ , and the longitudinal invariant J . Here

$$J = \oint V_{\parallel} dl.$$

In general, J is a function of magnetic flux lines and is dependent on the particle's energy and magnetic moment. Fig. 7a. shows the trajectory of a 360 keV deeply trapped electron in the Constance B magnetic field. The electron orbit drifts across magnetic field lines along a baseball seam curve while bouncing back and forth in the axial direction. The drift frequency is about 5 MHz. The vacuum magnetic field is used in the calculation and only the guiding center positions are plotted. Note that this drift orbit is very similar to the plasma profile observed in the experiment. On a time scale long compared with

the drift time, the particle is observed drifting on a nearly closed magnetic flux surface. Fig. 7b. shows the intersection of these flux lines at the midplane. It is a diamond shaped curve and it shows the shape of constant J surfaces in a quadrupole magnetic field. The numerical calculations also show that these constant J surfaces are only weakly dependent on the particle energy, pitch angle and mass. Since the particle drift surfaces are similar, we can pick a single drift surface for all the particles on that surface.

Similar characteristics emerge from studying the fluid equations. The MHD equilibrium of a magnetically confined plasma is maintained by balancing the plasma pressure with the forces resulting from the interaction of the plasma current and the applied magnetic field. In a magnetic mirror, the equilibrium relation is described by the guiding center fluid equations.

$$\vec{J} \times \vec{B} = \nabla \cdot \mathbf{P}$$

$$\nabla \times \vec{B} = \vec{J}$$

$$\nabla \cdot \vec{B} = 0.$$

Here $\mathbf{P} = P_{\perp} \mathbf{I} + (P_{\parallel} - P_{\perp}) \vec{b} \vec{b}$ is the anisotropic plasma pressure tensor. From these equations, the self-consistent magnetic field \vec{B} can be determined when the plasma pressure and the boundary conditions are known. The plasma pressure tensor itself, however, is a free function in the equations. It will be determined from the experimental measurements.

The force along a magnetic field line is balanced within the plasma pressure tensor itself. It requires

$$P_{\perp} = P_{\parallel} - B \frac{\partial P_{\parallel}}{\partial B},$$

where the derivative of P_{\parallel} is taken along a magnetic field line. With this relation, there is only one pressure function left to be determined from experiment.

Perpendicular to the magnetic field lines, the force balance can be written as

$$\nabla_{\perp} \left(\frac{B^2}{2} + P_{\perp} \right) = (B^2 + P_{\perp} - P_{\parallel}) \vec{\kappa},$$

where $\vec{\kappa} = (\vec{b} \cdot \nabla) \vec{b}$ is the magnetic field line curvature. Considering the equation in the \vec{b} , $\vec{\kappa}$ and $\vec{b} \times \vec{\kappa}$ directions, we see that $(\frac{B^2}{2} + P_{\perp})$ is constant in the $\vec{b} \times \vec{\kappa}$ direction. When the vector $\vec{b} \times \vec{\kappa}$ forms a closed flux surface, the plasma pressure profile will be a function of the magnetic field magnitude B and a single flux surface parameter. We need to evaluate the magnetic field geometry to determine this flux surface parameter.

In the low beta limit, the $\vec{b} \times \vec{\kappa}$ direction evaluated at the minimum of B corresponds to the drift orbit of particles deeply trapped near the magnetic minimum on each field line. This follows from the relation

$$\vec{\kappa} = (\nabla_{\perp} B + \vec{J} \times \vec{b}) / B.$$

When the plasma current density is small due to low beta, $\vec{\kappa}$ is parallel to $\nabla_{\perp} B$. Thus, a surface constructed by connecting all the flux lines which have the same minimum magnetic field value will correspond to the drift surface for a deeply trapped particle. We label such a surface as a constant J_* surface. The value of J_* is defined to be equal to the radius of the flux surface at 45 degrees at the midplane. The minimum B points on a constant J_* surface will form a baseball seam curve on a mod- B surface. It is easy to see that a deeply trapped plasma profile will peak along the magnetic field lines at these minimum B points. Therefore, as long as its radial profile is hollow, a baseball seam plasma will be formed.

In a finite beta plasma equilibrium, the magnetic field will be modified by the plasma current. So the $\vec{b} \times \vec{\kappa}$ direction is dependent on the plasma pressure profile and beta. However, it can still be shown that there exists a closed flux surface which is connected by the $\vec{b} \times \vec{\kappa}$ vector near the magnetic minimum on those field lines. Also, it has been observed in numerical equilibrium calculations that the change of $\vec{\kappa}$ and \vec{b} is usually small

compared with the change of ∇B .¹⁶ Based on this understanding, we assume that the plasma pressure has a functional structure $P_{\parallel,\perp} = P_{\parallel,\perp}(B, J_*)$, with J_* a constant on a vacuum field constant J surface. The use of $\vec{b} \times \vec{\kappa}$ near the magnetic minimum to determine the flux surface is justified by the fact that the plasma pressure profile has been experimentally observed to be very anisotropic and deeply trapped.

In principle, the equilibrium can be calculated when the pressure profile is given. But because of the nonlinear nature of the equations and the complicated magnetic geometry involved, the calculation is difficult to perform. Two approximations are used in the analysis:

(1) In a non-axisymmetric mirror field, there is a current flow along magnetic field lines if $\nabla \cdot \vec{J} = 0$ cannot be satisfied by \vec{J}_\perp alone. This condition can be expressed as

$$\vec{b} \cdot \nabla \left[\left(1 + \frac{P_\perp - P_\parallel}{B^2} \right) \frac{J_\parallel}{B^3} \right] + \frac{\vec{b} \times \vec{\kappa}}{B^2} \cdot \nabla (P_\perp + P_\parallel) = 0.$$

This equation shows that parallel currents exist whenever there is a non-zero pressure gradient along the $\vec{b} \times \vec{\kappa}$ direction. This current flows along the magnetic field line direction and changes the direction of the flux lines. However, the parallel current is not important for the equilibrium of a short-fat mirror like Constance B, where components of the much larger perpendicular current spread in all directions because of the magnetic flux fanning and make the parallel current a minor effect. The parallel current effect will become significant only when the device is long. Therefore, we have neglected the parallel current in our analysis.

(2) Because the Constance magnetic geometry is not long-thin, the paraxial approximation cannot be applied to the equilibrium analysis. The basic assumption of the paraxial approximation is that the plasma is confined in a region where the radial scale length is small compared with the axial scale length, and the magnetic field is primarily in the axial direction. In the Constance magnetic well, the plasma is generated with microwaves and exists in regions defined by the resonant mod-B surfaces. The ratio between the

radial and axial extent of these mod-B surfaces is about 1:1.6, and is roughly constant to the radius of these surfaces. So the long-thin approximation is not satisfied even at high field shots in which the plasma radial size is small. Without the long-thin approximation, our equilibrium analysis has been forced to rely largely on computational studies. With the amount of data needed to be calculated for comparison with the experimental measurements and determining the equilibrium, the computational requirements are too large for a self-consistent solution. Therefore, we used the vacuum field in the calculation instead of a self-consistent equilibrium magnetic field.

An accurate analytical magnetic field expression has been derived and used in the experiment simulation. In deriving the expression, we first solved Maxwell equations in a current free region and expressed the general solution in terms of a multipole expansion in cylindrical coordinates. The solution provided a general structure of multipole magnetic fields, with one free function for each multipole component. The free functions are then determined based on the magnetic field calculated with the EFFI code.¹⁷ The results are accurate to within 5 % in the entire plasma confinement region (mirror ratio 1.8). Details of the magnetic field expression and the derivation are given in the Appendix.

B. Plasma Profile Modelling

Based on the equilibrium properties discussed above, the structure of the plasma pressure profile is assumed to be $P=P(B, J_*)$. We further assume that the pressure can be expressed as separable functions, $P_{\perp}(B, J_*) = P_1(B) \cdot P_2(J_*)$. This assumption corresponds to the situation where the particle distribution function, apart from an overall weighting function, is the same on all field lines. There is no physics reason to believe it is necessarily true. The only reason for doing this is to simplify the analysis.

The function P_1 is taken to be

$$P_1(B) = \frac{nB^2(B_{max} - B)^{n-1}}{1 + e^{k(B-B_*)}}$$

This expression modifies Taylor's expression with a Fermi distribution function so that the pressure cutoff at the ECRH resonant mod-B surface can be modeled. In the expression, B_{max} is the maximum magnetic field at the mirror peak, and B_h the one half cutoff point in the Fermi distribution function. The parallel component of the pressure tensor, $P_{||}$, is calculated from P_{\perp} through the parallel force balance equation.

For P_2 we take

$$P_2(J_*) = \frac{1}{P_1[B_0(J_*)]} \times \begin{cases} p_0 + \sum_{n=2}^4 a_n J_*^n & \text{if } J_* \leq J_p \\ p_p e^{c_1(J_* - J_p)^2} & \text{if } J_* > J_p \end{cases}$$

Here, $B_0(J_*)$ is the minimum magnetic field on the drift surface J_* . With the factor $1/P_1(B_0)$, the radial effect of $P_1(B)$ is compensated. The net radial profile is then determined by the functions apart from $1/P_1(B_0)$. Inside the peak pressure point J_p (see Fig. 8), the profile is chosen so that $P_2(J_*) = p_0, p_1, p_p$ at $J_* = 0, J_1, J_p$, respectively. Outside J_p , a Gaussian function is used. We define the "hollowness" of the plasma to be $(p_p - p_0)/p_p$. The quantities p_0, p_1, p_p and J_1, J_p, c_1 are input parameters and the coefficients a_2 to a_4 are obtained with a linear equation solver which fits all the points and lets the slope at J_p to be zero. When this plasma profile model is used to simulate the hot electron density in analyzing the plasma visible light and x-ray images, we cut the plasma edge at the constant J_* surface on which $B_0(J_*)$ equals the resonant magnetic field so that the shape edge there can be modelled.

Even through this plasma model may seem very restrictive, because it contains both the physics feature of the plasma equilibrium and the confining magnetic geometry, a large variety of plasma pressure profiles needed for the equilibrium analysis can be modelled.

V. Experimental Observations

In the last two sections, the plasma equilibrium structure has been qualitatively presented and analyzed. The experimental data shows that the plasma is concentrated in a baseball seam curve, and it is formed by a deeply trapped plasma whose radial profile is hollow. Based on these observations and analysis, we developed a plasma pressure model. In this section, we analyze the experimental data from four independent measurements to determine the parameters in the model so that a quantitative determination of the plasma pressure profile can be obtained. One of the most important parameters we want to determine is the plasma hollowness. In a minimum-B magnetic field, a hollow plasma is expected to be MHD unstable. Thus the hollowness and the pressure gradient in the hollow region are crucial to stability analysis.

A. Visible Light Images

In a plasma, visible light radiation is emitted when an electron makes a transition in the field of an atom or ion. The three main transition processes are electron excitation, recombination, and bremsstrahlung radiation (free-free transitions). In a low density plasma, electron excitation is the predominant light source.

The visible light image of the plasma is measured with a CCD TV camera system which is sensitive to the spectral range from 400 to 1000 nm. The images after the ECRH is turned off are used for the hot electron density profile analysis. During the ECRH pulse, both the cold and the hot electron plasma densities are about $2 \times 10^{11} \text{ cm}^{-3}$ and the visible light radiation is determined by the cold electrons.

After the ECRH is off, the plasma becomes an almost completely hot electron plasma within a few hundred microseconds. The cold electrons are scattered into the loss cone on a time scale of $50 \mu\text{s}$, while the hot electron confinement time is about 2 seconds. The density of the cold electrons generated by hot electron ionization of the background

gas is on the order of one thousandth of that of the hot electrons. The neutral target density is spatially uniform at this time. The mean free path of the neutrals is about 50 cm, which is five times the plasma radius. Since the ratio of the excitation rates for cold electrons (100 eV) and hot electrons (≥ 100 keV) is on the order of 10, the visible light emission is primarily due to the hot electrons. In addition, the excitation cross-section to atomic and molecular hydrogen is a weak function of electron energy in the energy range 100 – 500 keV,¹⁸ which is characteristic of the afterglow electrons, thus the visible light radiation intensity is proportional to the hot electron density.

Since the plasma cross section is not circular, we integrate the model plasma profiles along the line-of-sight of the cameras and compare the projections with the plasma images measured in the experiment. The plasma images shown in Fig. 4 are generated with this method and the profile parameters for the two models are

$$n = 5, k = 10., B_h = 1.15; p_0 = 1.4, p_1 = 1.2, p_p = 1., j_1 = 0.037, j_p = 0.064, c_1 = 2000,$$

and

$$n = 5, k = 10., B_h = 1.2; p_0 = 0.5, p_1 = 0.75, p_p = 1., j_1 = 0.037, j_p = 0.064, c_1 = 500,$$

respectively.

A quantitative comparison is done by taking density traces from the photographs. Fig. 9 shows the film density traces measured from the visible light photograph which has been presented in Fig. 3a. The simulated line integrations of the 50 % hollow hot electron density profile (see Fig. 4b.) are plotted in dashed lines. To show the sensitivity of this comparison, line integrations from a 60 % hollow profile are also plotted with the radial density traces. The parameter difference between the two modelled profiles is that p_0 is changed from 0.5 to 0.4 and p_1 from 0.75 to 0.7. Note that this 10 percent difference in the hollowness can be distinguished. The axial plasma profiles are analyzed by taking density traces parallel to the magnetic axis. Fig. 9b. shows the density traces of the plasma image at two radial locations ($x=0, 5.7$ cm). The dashed lines are from the line

integral of the 50 % hollow profile.

The errors involved in this analysis mainly come from the hot electron temperature non-uniformity and the camera viewing angle. The line-of-sight from the plasma edge to the camera is 12 degrees with respect to the x-axis. The error induced is less than 3 percent. The error due to the temperature non-uniformity is within 5 percent in the hot electron temperature range, which is between 100 – 500 keV.

From the visible light image measurement, we conclude that the best fit hot electron density profile is the one whose on axis dip is 50 %, with an accuracy $\pm 10\%$ (Fig. 4b.). This hot electron density profile should not be simply assumed to be the pressure profile because the hot electron temperature is not uniform.

B. X-ray Images

The x-ray emission from a hot electron plasma is primarily due to bremsstrahlung radiation. The radiation profile is proportional to the hot electron density times the target density, with a profile factor determined by the plasma temperature profile. The target density is mostly contributed by the ions, whose density is usually 20 times higher than the neutral gas density. From the soft x-ray spectrum measurements, it has been determined that impurity targets contribute about 20-30 % of the total x-ray flux. Because the cold electron profile is less hollow than the hot electron profile according to the visible light image measurement during and after the ECRH pulse, the ion density profile is somewhere between the cold and hot electron profile. To make a quantitative comparison, we assume the x-ray radiation intensity is proportional to n_{hot}^δ , with a δ value between 1.5 and 2. Here, $\delta = 2$ corresponds to the situation that the hot electron and the cold electron profiles are the same, and $\delta = 1.5$ corresponds to a nearly flat cold electron density profile. Since the x-ray images measured at different energy ranges are very similar, no further temperature dependence is assumed.

Fig. 10 shows the x-ray film density traces measured from the x-ray photograph which was presented in Fig. 3c, together with two simulated density traces using the two radiation profile models. With $\delta = 1.5$ (dotted line), the best fit plasma profile is a 60 percent hollow profile with parameters

$$n = 7, k = 10., B_h = 1.18; p_0 = 0.4, p_1 = 0.7, p_p = 1., j_1 = 0.035, j_p = 0.064, c_1 = 900.$$

With $\delta = 2$, the best fit profile is the one whose on axis dip is 50 percent with

$$n = 6.2, k = 10., B_h = 1.19; p_0 = 0.5, p_1 = 0.75, p_p = 1., j_1 = 0.035, j_p = 0.064, c_1 = 600.$$

The radial distributions of these two plasma density profiles are plotted in Fig. 11, together with the hot electron density profile determined from the visible light photographs. Both the x-ray and the visible light images show that the hot electron density is peaked at $J_* = 6.4$ cm, and the hollowness of the profile is about 50 percent. The difference between these three curves is less than 10 percent, with is in very good agreement considering the uncertainties in the x-ray imaging analysis, such as impurity profile and hot electron temperature profile effects.

C. Magnetic Measurements

Extensive magnetic measurements have been done to determine the plasma pressure profile. The plasma magnetic field is measured with diamagnetic loops and magnetic probes. Ratios between these magnetic signals are used in the equilibrium determination since they are independent of the total stored energy. There are only a few positions where the magnetic signals are sensitive to the plasma pressure profile change. We determined these locations and the magnetic field components from experiments and the numerical calculations.

To interpret the measured plasma magnetic field, the plasma current density is calculated from the equilibrium force balance equation

$$\vec{J}_\perp = \frac{\vec{B} \times [\nabla_\perp P_\perp + (P_\parallel - P_\perp)\vec{\kappa}]}{B^2}.$$

We then calculate the magnetic signals for different plasma pressure models and compare the predictions with the measurements. The frequency response of the magnetic probes is measured inside the the vacuum chamber. The effect of the aluminum wall is measured to be less than 2 % at frequencies below 5 Hz. So the vacuum boundary condition is used in the calculation.

There are eight independent parameters in the pressure profile model. To analyze the amount of data which comes from such a multi-dimensional parameter space, it is important to organize the data well so that the analysis can be systematically conducted and a reliable result be obtained. We use a graphic method to present the data in the analysis.

Fig. 12 presents the calculated ratios between the signals of the midplane diamagnetic loop and a B_x probe at $r = 15.2$ cm on the midplane from 81 model plasma profiles. The data is organized into 9 boxes. Inside each box, the horizontal axis is J_p , which represents the radius of the plasma pressure peak; the vertical variable is p_0 , which reflects the hollowness on the magnetic axis. Between the boxes, the horizontal variable is c_1 , which determines the sharpness of the plasma edge; in the vertical direction, three $P_1(B)$ profiles are represented. By presenting the data in this way, four dimensional variations of the pressure profile parameters can be analyzed simultaneously. The trend of the signal change with the plasma profiles and the sensitivity of the signal to various pressure models are also clearly seen.

The signal presented in Fig. 12 is the signal which is most sensitive to the radial pressure profile change. The signal measured by the midplane diamagnetic loop is dominated by the plasma dipole field. The B_x probe senses the quadrupole field only since the x-component of the dipole field is cancelled at the midplane. The quadrupole field is generated because of the magnetic field fanning, which increases with the radius. Thus, the ratio between the dipole and the quadrupole signals is a measure of the plasma current

radial location.

From the data presented in the figure, however, it is clear that this measurement is much more sensitive to the outer plasma profile than to the profile near the magnetic axis. With the value of J_p varying from 5 to 7 cm, the change of the signal ratios varies by 30 to 50 percent. One can clearly distinguish that the best fit J_p is near 6 cm. Unfortunately, the pressure profile near the magnetic axis cannot be determined from these data. Despite variations in the hollowness from 70 % hollow to 20 % peaked, the difference in the magnetic signal is only about 10 - 20 %. One can imagine that if contours of constant loop to probe signal ratio are drawn inside each data box, these curves will be nearly vertical lines. When the measured signal ratio is compared with these predicted ratios, only the plasma outer radius can be determined. Other magnetic signals are all similar in this respect because the plasma volume near the axis is small and the coupling to the probe is weak compared with that of the outer plasma. Considering that the measurement accuracy of the diamagnetic probes is about 5 percent, and that several approximations have been used in the numerical simulation, we estimate that the accuracy of the magnetic analysis is about 10 percent. We conclude that the magnetic measurements cannot be used to accurately determine the plasma hollowness.

An estimate of the hollowness of the plasma pressure profile can be obtained from the diamagnetism change in the skimmer probe radial scan. When a skimmer probe intersects a field line at an axial position inside the ECRH resonant surface, the probe blocks the access to the resonance zone for electrons on that field line. It also wipes out the plasma on that drift surface as the particles drift around the magnetic axis. As seen in Fig. 1, the ECRH resonant surface in Constance is egg shaped, and the resonance for field lines near the axis extends to large z . Thus we can affect the radial plasma pressure profile by inserting a skimmer probe off the midplane, which reduces the pressure on axial field lines while barely affecting the outlying plasma. By modelling the diamagnetism

change between the perturbed pressure profile and the unperturbed pressure profile with varying degrees of hollowness, an estimate of the hollowness of the plasma pressure can be obtained when the predictions are compared with the measurements. The data presented in Fig. 5 is the diamagnetic signal vs. a skimmer probe inserted along the line at $z = -10$ cm in the horizontal symmetry plane. We model the effect of the skimmer probe by assuming that on field lines outside the resonance zone the plasma pressure is not affected by the probe, and once the probe penetrates the resonance zone the pressure on the drift surfaces which contact the probe is reduced to zero. We then take the ratio between the diamagnetism predicted by this model with the diamagnetism predicted by the models with varying degrees of hollowness on the axis. This ratio gives an indication of the expected decrease of diamagnetism due to the insertion of the probe as function of the hollowness of the unperturbed plasma. The calculation shows that if the pressure profile is originally 80 percent hollow, the diamagnetism will drop by about 21 % after the skimmer probe is inserted. If the original profile is 50 percent hollow, the drop of diamagnetism will be 29 %. The experimental data shows that as the probe is inserted the diamagnetism decreases by about 12 percent until the probe is 2 cm from the axis when it abruptly decreases to 50 percent of its original value. This final abrupt drop we interpret as due to the droop of the probe below the horizontal symmetry plane on the basis of other skimmer probe scans in which the probe is deliberately moved off the symmetry plane. Another possible explanation for the final drop would be the existence of a high pressure plasma column of radius 2 cm on the axis. However, given the fact that the peak plasma temperature is about 400 keV, one would expect the hot electron density there to be at least 10 times higher than the density at the outer peak pressure location ($J_p = 6$ cm). This prediction directly contradicts the x-ray and visible light image measurements. The thermocouple mounted on the tip of the skimmer probe also shows that the plasma energy on the axis is a minimum rather than a maximum. Therefore such a high density

column does not exist. Based on the measured diamagnetism change, we can say that the pressure profile is at least as hollow as, if not more hollow than the hot electron density.

To determine the outer radial profile, we set the hollowness to be 50 percent according to the hot electron density, and then vary the other profile parameters. The exact value of the hollowness is not crucial in determining the outer profile since its effect is small. Because most of the magnetic signals are affected by the outer profile change, we started the calculation with a wide parameter regime to include all the possible profiles. The predictions from the model profiles are compared with the experimental data to determine the best fit parameter region. The next round of calculations is then conducted in this region with refined grids. When the pressure profiles converge to the region corresponding to the 5 percent experimental accuracy, a χ^2 test is used to determine which profile has the least deviation from the measurement.

The axial pressure profile is determined from the ratio between the midplane diamagnetic loop and other pickup loops and probes at different axial locations. The overall plasma length is monitored by an elliptical diamagnetic loop at $z=22$ cm. Fig. 13 shows the calculated ratios between the midplane loop and the elliptical loop signals for 5 different $P(B)$ profiles. It shows that the bulk of the plasma is within mirror ratio 1.2, which corresponds to an axial extent of $z=14$ cm. The plasma pressure drops to less than 5 percent outside the the ECRH resonance mirror ratio 1.25. More detailed analysis is made with the magnetic probes at $z=10$ and 20 centimeters. When the probes are close to the plasma, they are mostly sensitive to the local pressure profile. Taking the ratio between the diamagnetic loop and the probe signals, the relative plasma pressure at the probe axial location can be determined. These data are relatively insensitive to the radial pressure profile change. After having analyzed all the magnetic measurements, we conclude that the best fit plasma pressure profile is the one defined by the parameters $n = 4.5, k = 40., B_h = 1.19; p_0 = 0.5, p_1 = 0.75, p_p = 1., j_1 = 0.035, j_p = 0.06, c_1 = 3000.$

The best fit radial pressure profile is plotted as the solid line in Fig. 11 together with the density profiles determined from the visible light and x-ray image measurements. Notice that the plasma radial pressure profile is smaller than the hot electron density profile. The peak pressure is at $J_r = 6$ cm and the peak hot electron density is at 6.4 cm, and the pressure drops more quickly outside the peak position. This difference between the hot electron density and pressure profiles indicates the plasma temperature is colder at the plasma edge, which agrees with the x-ray spectroscopic measurements.

D. Thermocouple Probe Measurement

The plasma radial boundary and the end loss profile are measured with thermocouple probes. The probes are inserted into the plasma to measure the local plasma energy. During the ECRH pulse, the probe draws a plasma current since its circuit is similar to a Langmuir probe. We measure the probe temperature difference before and after the ECRH pulse to obtain the time averaged plasma energy profile. The time response of the probe is about 2 seconds, which makes such a measurement possible.

The thermocouple probe is the most sensitive diagnostic in determining the plasma boundaries. Fig. 14 shows the thermocouple temperature profile measured at three axial locations ($z=0, 10, 20$ cm). All the data points are mapped back to the midplane along the magnetic flux lines so that measurements at different axial locations can be compared. It shows that the hot electron plasma exists only on the field lines on which the nonrelativistic electron cyclotron resonance occurs. It should be remembered that the data points do not correspond to the plasma pressure profile because the plasma is perturbed when the probe is pushed into the plasma.

At $z=20$ cm, the thermocouple probe can be used to scan across the entire magnetic flux tube. At this position, the probe is measuring the particles at large pitch angle, and their energy distribution may be different from the bulk of the plasma. However, since

the probe acts as an axial plasma limiter, the measured energy profile is the end loss profile and is equal to the ECRH energy deposition profile during a steady state shot. The data shows that the energy profile is 90 % hollow. Considering that the plasma width at this axial location is only 2.5 cm and the hot electron Larmor radius is 0.6 cm, the end loss profile should be more sharply peaked than these data show. The measured peak temperature position corresponds to the field line with 12 cm radius at the midplane. This peak position is not on the field line tangent to the resonant surface but on a line which is inside and has a vacuum field ECRH resonant mirror ratio of 1:1.06 (see Fig.1). To determine the thickness of the layer where most of the ECRH power is absorbed, one can follow the field lines back to the hot electron confinement region. The data shows that 90 percent of the ECRH power is absorbed in the region where the hot electrons peak and the thickness of this layer is about 4-4.5 cm, which is about 6 to 7 hot electron gyroradii.

Up to this point, we have concentrated on the analysis of the plasma equilibrium under the standard operating condition. We determined the hot electron plasma density profile from visible light and x-ray images. The axial and outer radial pressure profiles are determined from the magnetic measurements. The plasma boundary and the ECRH power deposition profile is measured with the thermocouple probe. The plasma pressure is peaked near $J_z = 6$ cm and the hollowness of the pressure is at least 50 percent.

E. Variation of Equilibrium with Experimental Conditions

The characteristic baseball seam plasma equilibrium is observed under all experimental conditions in which the equilibrium has been measured, ranging from magnetic fields of 2.8-3.75 kG, ECRH microwave power from 10 W to 4 kW, and neutral gas pressure varying from 2×10^{-7} to 4×10^{-5} Torr.

In a magnetic field scan, the plasma size is observed to scale with the ECRH resonance surface size but the baseball seam equilibrium structure remains. Fig. 15 is an x-ray

pinhole photograph taken in a $B_0 = 3.6$ kG shot. It shows that the plasma radius is reduced to about 4.5 cm, and the "C" structure can be clearly seen. An ECRH resonance inside the magnetic well is required for gas breakdown. With the vacuum magnetic field settings at $B_0 = 3.75$ kG, no plasma can be generated. When the field is lowered by only 5 Gauss, high beta steady state plasmas ($\beta_{peak} = 0.5$) can be produced. When the midplane magnetic field is larger than 3.5 kG, plasma expansion is observed with the visible light TV cameras. In the $B_0 = 3.6$ kG shot, the plasma radius is about 3.5 cm at the beginning of the shot and it expands with the increase of the total stored energy. It takes about 1 second for the radius to expand to 4.5 cm and reach steady state. This expansion during the shot is believed to be due to diamagnetic depression. It is observed only at the bottom of the magnetic well where the gradient of the magnetic field is small. If it were due to the hot electron relativistic resonance shift, one would expect that the expansion would occur in all the cases when the hot electron temperature is at several hundred kilovolts.

In the neutral gas pressure and ECRH power scans, plasma length contraction during ECRH heating is observed. The plasma starts with a shallow profile at the beginning of a shot and then becomes more and more deeply trapped before the profile reaches a steady state. The speed of the contraction and the final state are dependent on the neutral gas pressure and the applied ECRH power. In general, the speed of the contraction increases with increasing ECRH power or decreasing gas pressure, and the steady state plasma length decreases with increasing ECRH power and decreasing gas pressure. At low gas pressure (below 1×10^{-6} Torr) and moderate ECRH power (2 kW), the plasma length changes by 2 to 3 cm in about 0.1 seconds and the steady state plasma profile is reached before the plasma beta reaches its peak value. At high gas pressure, the contraction process is much slower. With gas pressures above 5×10^{-6} Torr, steady state pressure profiles are not reached in the 2 seconds long shots. The plasma length in the final state

is more sensitive to the ECRH power than the neutral gas pressure.

The plasma axial length is determined by the particle pitch angle distribution. For an ECRH generated plasma, electrons get perpendicular "kicks" from the resonance rf field and turn to become more deeply trapped. However, the electrons also get parallel "kicks" from rf diffusion and microinstabilities, as well as Coulomb collisions. The balance between these two processes determines the equilibrium distribution function. Therefore the plasma length change during ECRH is not unexpected. But to understand the behavior of the plasma profile change, the diffusion processes in velocity space have to be carefully analyzed, and this is beyond the scope of this paper.

VI. Discussion

With the equilibrium pressure profile determined, several plasma properties can be analyzed.

(1) One important feature of the plasma pressure is that the bulk of the plasma is confined inside the ECRH resonant surface. To relate this pressure profile to the underlying pitch angle distribution function, one can take an Abel inversion of the plasma pressure profile $P_{\perp}(B)$.^{19,20} However, it is more instructive to directly integrate some commonly used velocity distribution functions and compare them with the measurement. Fig. 16 shows the experimentally determined $P_{\perp}(B)$ profiles and the ones calculated from a bi-Maxwellian loss cone and an ECRH loss cone⁹ distribution. With the bi-Maxwellian loss cone distribution, the pressure profile is always sharply peaked at the magnetic minimum. With a distribution function which is nearly flat inside the ECRH heating line, the corresponding pressure profile is much closer to the measured one.

(2) A primary motivation of the hot electron plasma study is that hot electrons may be used to produce minimum B in an otherwise unstable magnetic configuration. We calculated the magnetic field gradient ∇B for standard operating conditions, using the

equilibrium relations which are expanded to the first order in beta and assuming that the magnetic field curvature change is small compared with the change of ∇B . The calculations show that for the most smooth radial functions the gradient reversal occurs at beta values of about 20, 23, and 27 percent for plasma pressures with hollowness 60, 50, and 40 percent. In the experiment, 30 % beta is regularly achieved with 2 kW of applied microwave power. In the 4 kW shots, more than 40 % beta has been generated. Thus we conclude that magnetic field gradient reversal is achieved. One should notice that the stability of the plasma is not dependent on the gradient reversal since the plasma is observed to be stable at all beta values.

The particle drift in the equilibrium magnetic field is expected to be reversed when magnetic gradient reversal occurs. Berk and Zhang²² have analyzed the plasma stability near drift reversal with a model in which the magnetic field lines are straight and there is a rigid embedded current to simulate the effect of curvature, assuming a sharp edged pressure profile. They predicted that there is a "precessional layer" mode which is unstable before the onset of the drift reversal. Hiroe²³ has suggested that there would be strong radial diffusion when the drift reversal occurs because the particle drift direction is not well defined in this situation. We have calculated the bounce averaged hot electron drift frequency in the equilibrium magnetic field, using the guiding center drift velocity

$$\vec{v}_d = \frac{\vec{b}}{qB} \times (\mu \nabla B + m\gamma v_{\parallel}^2 \vec{\kappa}).$$

Fig. 17 shows the drift frequency in the 30 percent beta equilibrium field. The distances between the turning points of the electron bounce motions are from 7 to 11 cm, which is about a quarter of the plasma axial length. It shows that for the particles on field lines inside the peak pressure position, the drift is reversed. One may expect some macroscopic plasma change associated with the transition when the particles change their drift from one direction to the other. However, this is not observed in the experiment.

(3) With a high beta, deeply trapped plasma equilibrium, it is interesting to see if the

mirror mode beta limit is approached. The mirror mode stability condition²¹ is given by

$$\tau = 1 + \frac{1}{B} \frac{\partial P_{\perp}}{\partial B} > 0.$$

Beyond this limit, MHD equilibrium becomes an ill-imposed problem.¹⁹ The most anisotropic plasma profiles are obtained in the high magnetic field shots. When the midplane magnetic field is 3.6 kG, the vacuum field ECRH resonant surface extends only to $z=6.5$ cm and the resonance mirror ratio is 1:1.04. Without the plasma diamagnetic depression, the mirror mode limit is about $\beta = 0.08$. However, the plasma beta is measured to be about 50 percent in the experiment. In such a high beta plasma, the magnetic field geometry is strongly modified by the plasma currents and the diamagnetic depression must be taken into account. To the first order approximation in beta, numerical calculations show that a 600 Gauss diamagnetic field is generated at the peak pressure position. This pushes the beta limit to about 40 percent, which is very close to the required diamagnetic depression to have the mirror mode limit satisfied. Thus a nonlinear analysis is needed to determine if the stability condition is violated. When the mirror mode beta limit is so closely approached, one may expect particle adiabaticity loss or some turbulence to occur. The only experimental evidence related to this is the plasma radial expansion observed under such conditions. However, it is more reasonable to believe that the expansion is due to plasma diamagnetism rather than the loss of adiabaticity because the expansion starts early in a shot before the mirror mode beta limit is reached. It is not clear at this point if the plasma beta is limited by this stability condition.

(4) The hollow plasma equilibrium has been observed to be macroscopically stable, and the stability is independent of the plasma beta, electron temperature, and the background neutral gas pressure. A hollow plasma in a minimum B magnetic configuration is expected to be MHD unstable. With the plasma equilibrium profile determined, the stability conditions from many theoretical studies can be quantitatively analyzed and tested. We will discuss the stability issue in a separate paper.

VII. Summary

We have quantitatively determined the equilibrium plasma profile of an ECRH generated hot electron plasma in a minimum-B baseball magnetic mirror using four complementary measurements, including x-ray imaging, visible light imaging, magnetic and thermocouple measurements. The primary results are: (1) An ECRH generated hot electron plasma in a minimum-B quadrupole magnetic mirror is hollow. The plasma is confined along a baseball seam curve inside the non-relativistic ECRH resonant surface. This baseball seam equilibrium profile coincides with the drift orbit of deeply trapped electrons in the quadrupole magnetic field. (2) Under the standard operating conditions of Constance ($B_0=3$ kG, ECRH power=2 kW, gas pressure= 5×10^{-7} Torr, and plasma beta=0.3), the hollowness of the hot electron plasma density profile is 50 ± 10 percent, and the plasma pressure is at least as hollow as the hot electron density. The thickness of the hot electron layer is about 4 - 4.5 cm, or 6 - 7 hot electron Larmor radii. (3) The hollow plasma equilibrium is macroscopically stable. It is generated in all the experimental conditions in which equilibria have been measured, ranging from $B_0 = 2.8 - 3.74$ kG, ECRH power=10 - 4000 W, and neutral gas pressure= $2 \times 10^{-7} - 5 \times 10^{-5}$ Torr. (4) Particle drift reversal is achieved in the experiment. There has been no evidence that the plasma becomes unstable when the drift reversal occurs. (5) At high magnetic field shots ($B_0 \geq 3.5$ kG), the mirror mode beta limit is closely approached. Further analysis is needed to determine if the plasma beta is limited by this stability condition.

Acknowledgments

The authors wish to thank D.L Goodman, C.C. Petty and R.C. Garner for their cooperation in the experiment. We also wish to acknowledge many helpful discussions with S. Hiroe, J. Kesner, M. Gerver and D.K Smith, and to thank K. Rettman for his technical support. This work was supported by the U.S. Department of Energy, Contract

No. DE-AC02-78ET51013.

Appendix: An Analytic Approximation of the Constance B Magnetic Field

An analytical approximation of the Constance B magnetic field is derived for the equilibrium analysis. In deriving this expression, we first solve the Maxwell equations for a vacuum magnetic field and obtain the general solution in terms of multipole expansions. We then apply the solution to Constance B where the magnetic field is dominated by dipole and quadrupole fields. By matching the undetermined functions in the general solution to the fields calculated with the EFFI code and keeping the radial function to the order of r^4 , we obtained an expression which is accurate to within 5 percent in the entire plasma confinement region ($\frac{B}{B_0} \leq 1.8$).

1. General Structure of Multipole Magnetic Field

A vacuum magnetic field can be solved in terms of an expansion series in cylindrical coordinates. We start from the Maxwell equations for a current-free magnetic field and let $\vec{B} = \nabla\chi$. Then χ satisfies the Laplace equation $\nabla^2\chi = 0$. Expanding χ into multipole components in cylindrical coordinates

$$\chi = \sum \chi_k(z, r) \cos(k\phi) \quad k = 0, 2, 4, \dots$$

the Laplace equation takes the form

$$\left(\frac{1}{r} \frac{\partial}{\partial r} r \frac{\partial}{\partial r} - \frac{k^2}{r^2} + \frac{\partial^2}{\partial z^2} \right) \chi_k = 0. \quad (1)$$

Then expanding χ_k into a power series in r

$$\chi_k = \sum_{n=0}^{\infty} g_{k,n}(z) r^n,$$

Eq. (1) becomes

$$\sum_{n=0}^{\infty} \left[(n^2 - k^2) r^{n-2} + r^n \frac{\partial^2}{\partial z^2} \right] g_{k,n} = 0. \quad (2)$$

By matching the coefficients of each r^n , we have

$$g_{k,n+2} = -\frac{g''_{k,n}}{(n+2)^2 - k^2} \quad n = k, k+2, \dots \quad (3)$$

Where $g''_{k,n}$ denotes the derivative with respect to z . It is clear that there is only one free function for each multipole component, which is the first term in that series. All the later terms can be expressed in terms of the derivatives of the first term.

Now all multipole field components can be constructed. For a dipole field, the solution is

$$\chi_0 = (g_0 - \frac{1}{4}g''_0 r^2) + \frac{1}{64}g_0^{(4)}r^4 - \dots \quad (4)$$

For a quadrupole field, the solution is

$$\chi_2 = g_2 r^2 - \frac{1}{12}g_2'' r^4 + \dots \quad (5)$$

Higher multipoles can be easily obtained in the same way. We have used $g_k(z)$ to denote $g_{k,k}(z)$, and $g_k^{(m)}$ to denote the m_{th} derivative of g_k .

In the so called long-thin approximation, one keeps the first terms in each multipole component. The result is

$$\chi = g_0 - \frac{1}{4}g_0'' r^2 + \sum g_k r^k \cos(k\phi) \quad k = 2, 4, 6, \dots \quad (6)$$

2. Constance B Magnetic Field

Constance B magnetic field is generated by a baseball magnet. It contains primarily dipole and quadrupole components. If one keeps the radial functions to the order of r^4 , the magnetic field can be expressed as

$$\begin{aligned} B_x &= (-\frac{1}{2}g_0'' + 2g_2)x + \frac{1}{16}g_0^{(4)}(x^2 + y^2)x - \frac{1}{3}g_2''x^3 \\ B_y &= (-\frac{1}{2}g_0'' - 2g_2)y + \frac{1}{16}g_0^{(4)}(x^2 + y^2)y + \frac{1}{3}g_2''y^3 \\ B_z &= g_0' - \frac{1}{4}g_0^{(3)}r^2 + \frac{1}{64}g_0^{(5)}r^4 + g_2'(x^2 - y^2) - \frac{1}{12}g_2^{(3)}(x^4 - y^4). \end{aligned} \quad (7)$$

The mod-B surface is of the form

$$B^2 = f_0^2 + f_1(x^2 + y^2) + f_2(x^2 - y^2) + f_3(x^4 + y^4) + f_4(x^4 - y^4) + f_5x^2y^2. \quad (8)$$

Here, $f_0 = g'_0$ is the magnetic field on the z axis. All the f functions are functions of g 's and their derivatives.

Analytical approximations of $g'_0(z)$ and $g_2(z)$ in Eq. (7) can be obtained when \vec{B} has been numerically calculated. However, a large quantity of data is needed in order to accurately determine all the higher order derivatives of $g_0(z)$ and $g_2(z)$. Thus we use another approach to derive the expression. We first fit the f functions in Eq. (8) to the mod-B contours calculated with EFFI code, and then determine the direction of \vec{B} from the field line trajectory. The resulting expression for the magnitude of the magnetic field can be simplified as

$$B^2 = f_0^2 + f_1[(x^2 + y^2) - 2(x^4 + y^4)] + f_2[(x^2 - y^2) - 2(x^4 - y^4)], \quad (9)$$

with

$$f_0 = 1 + 0.8[1 - \cos(5z)] - 59.z^6$$

$$f_1 = 52(1 + 10z^2) \cos(2z)$$

$$f_2 = -(120z + 1328z^3).$$

Where B is normalized to be one at the center of the mirror well, and x, y, z are expressed in meters.

The trajectory of a magnetic field line satisfies

$$\frac{dx}{B_x} = \frac{dy}{B_y} = \frac{dz}{B_z}. \quad (10)$$

In the long-thin approximation, this equation can be easily solved if there are only dipole and quadrupole fields. The solution is

$$x = x_0 \frac{1}{\sqrt{f_0}} e^{\xi(z)} \quad y = y_0 \frac{1}{\sqrt{f_0}} e^{-\xi(z)}, \quad (11)$$

where x_0 and y_0 are the field line positions on the magnetic midplane and $\xi = \int_0^z \frac{2g_2}{g_0} dz$. The numerically generated Constance magnetic field shows that the flux lines can be very closely approximated by $x = x_0\sigma(z)$ and $y = y_0\tau(z)$, with σ and τ some functions of z . This suggests that despite the fact that r^4 terms are needed to describe the magnetic field magnitude, the long-thin approximation for the field line trajectories can still be used. By fitting the trajectory functions of Eq. (11) to the calculated trajectories, we obtain

$$x = r_0 \cos\phi \frac{1}{\sqrt{f_0}} e^{(8.15-15.6z^2)z}, \quad y = r_0 \sin\phi \frac{1}{\sqrt{f_0}} e^{-(8.15-15.6z^2)z}, \quad (12)$$

where r_0 and ϕ denote the radius and the angular position of the field line at the midplane.

The three components of the magnetic field can then be calculated from

$$\begin{aligned} B_x &= \frac{x'}{\sqrt{1+x'^2+y'^2}} B \\ B_y &= \frac{y'}{\sqrt{1+x'^2+y'^2}} B \\ B_z &= \frac{1}{\sqrt{1+x'^2+y'^2}} B. \end{aligned}$$

The goodness of the fitting can be evaluated by the accuracy of the fitted expression with respect to the calculated field, and the magnitude of its divergence and curl relative to B/L , with L the scale length of the field. A numerical comparison shows that the expression is accurate to within 5 percent in the entire magnetic well, and that the divergence and the curl are typically a few percent of B/L , with $L = 40$ cm. Since there are only two independent functions g_0 and g_2 in the magnetic field expression, we can cross check the fitted expressions for f_1, f_2, f_3, f_4, f_5 and ξ by evaluating g_0 and g_2 from any two of them and then construct all the rest from g_0 and g_2 . The cross check shows that the f and ξ functions are in good agreement with the reconstructed functions and the differences between them are typically below 5 percent.

References

- ¹Taylor, J.B., *Phys. Fluids* **6**, 215 (1963).
- ²G.I. Dimov, V.V. Zakaidekov, and M.E. Kishinovskii, *Fiz. Plasmy* **2**, 597 (1976) [*Sov. J. Plasma Phys.* **2**, 326 (1976)]; Fowler, T.K. and B.G. Logan, *Comments Plasma Phys. and Controlled Fusion Research* **2**, 167 (1977).
- ³F.H. Coensgen, et al., *Phys. Rev. Lett.* **44**, 1132, (1980).
- ⁴T.C. Simonen, S.L. Allen, D.E. Baldwin, T.A. Casper, J.F. Clauser, F.H. Coensgen, R.H. Cohen, D.L. Correll, W.F. Cummins, C.C. Damm, J.H. Foote, T.K. Fowler, R.F. Goodman, D.P. Grubb, D.N. Hill, E.B. Hooper, R.S. Hornady, A.L. Hunt, R.G. Kerr, G.W. Leppelmeier, J. Marilleau, J.M. Moller, A.W. Molvik, W.E. Nexsen, J.E. Osher, W.L. Pickles, P. Poulsen, G.D. Porter, E.H. Silver, B.W. Stallard, J. Taska, W.C. Turner, J.D. Barter, T.W. Christensen, G. Dimonte, T.E. Romesser, R.F. Ellis, R.A. James, C.J. Lasnier, T.L. Yu, L.V. Berzins, M.R. Carter, C.A. Clower, B.H. Failor, S. Falabella, M. Flammer, T. Nash, and W.L. Hsu, *Plasma Physics and Controlled Nuclear Fusion Research*, 1984, London, United Kingdom (IAEA, Vienna, 1985), Vol. II, p. 255.
- ⁵R.S. Post, M. Gerver, J. Kesner, J.H. Irby, B.G. Lane, M.E. Mauel, B.D. McVey, A. Ram, E. Sevillano, D.L. Smatlak, D.K. Smith, J.D. Sullivan, J. Trulsen, A. Bers, J.W. Coleman, M.P.J. Gaudreau, R.E. Klinkowstein, R.P. Torti, X. Chen, R.C. Garner, D.L. Goodman, P. Goodrich, S.A. Hokin, *Plasma Physics and Controlled Fusion Research*, 1984, London, United Kingdom, (IAEA, Vienna, 1985), Vol. II, p.285.
- ⁶N. Hershkowitz, R.A. Breun, D.A. Brouchous, J.D. Callen, C. Chan, J.R. Conrad, J.R. Ferron, S.N. Golovato, R. Goulding, S. Horne, S. Kidwell, B. Nelson, H. Persing, J.

- Pew, S. Ross, G. Severn, and D. Sing, *Plasma Physics and Controlled Nuclear Fusion Research*, 1984, London, United Kingdom (IAEA, Vienna, 1985), Vol. II, p. 265.
- ⁷S. Miyoshi, T. Cho, M. Ichimura, M. Inutake, K. Ishii, A. Itakura, I. Katanuma, T. Kawabe, Y. Kiwamoto, A. Mase, Y. Nakashima, T. Saito, K. Sawada, D. Tsubouchi, N. Yamaguchi, and K. Yatsu, *Plasma Physics and Controlled Nuclear Fusion Research*, 1984, London, United Kingdom, (IAEA, Vienna, 1985), Vol. II, p. 275.
- ⁸D.L Smatlak, X. Chen, B.G. Lane, S.A. Hokin, R.S. Post, *Phys. Rev. Lett.* **58**, 1853 (1987).
- ⁹R.C. Garner, M.E. Mauel, S.A. Hokin, R.S. Post, D.L. Smatlak, *Phys. Rev. Lett.* **59**, 1821 (1987).
- ¹⁰R.A. Dandl, A.C. England, W.B. Ard, H.O. Eason, M.C. Becker, and G.M. Hass, *Nucl. Fusion* **4**, 344 (1964).
- ¹¹R.A. Dandl, F. W. Baity, et al., *Plasma Physics and Controlled Nuclear Fusion Research*, 1979 (IAEA, Vienna, 1979) Vol. II, p.365.
- ¹²B.H. Quon, R.A. Dandl, W. DiVergilio, G.E. Guest, L.L. Lao, N.H. Lazar, T.K. Samec, and R.F. Wuerker, *Phys. Fluids* **28**, 1503, (1985); C.L. Hedrick, L.W. Owen, B.H. Quon, and R.A. Dandl, *Phys. Fluids* **30**, 1860 (1987).
- ¹³M. Fujiwara, T. Kamimura, M. Hosokawa, T. Shoji, H. Iguchi, H. Sanuki, K. Takasugi, F. Tsuboi, H. Tsuchidate, K. Kadota, K. Sato, K. Tsuchida, A. Tsushima, and H. Ikegami, *Plasma Physics and Controlled Fusion Research* (IAEA, Vienna, 1985), Vol. II, p.551.
- ¹⁴G.R. Haste and N.H. Lazar, *Phys. Fluids* **16**, 683 (1973).
- ¹⁵Xing Chen, submitted to *Rev. Sci. Instrum.* (1987).

- ¹⁶D.A. Anderson, Private communication, (1985).
- ¹⁷Sackett, S.J., *Lawrence Livermore National Laboratory Report*, UCRL-52402 (1978).
- ¹⁸C.F. Barnett, J.A. Ray, E. Ricci, M. I. Wilker, E.W. MacDaniel, E.W. Thomas, and Gilbody, *Atomic Data for Controlled Fusion Research*, Oak Ridge National Laboratory, Oak Ridge, TN, ORNL-5207 (1977).
- ¹⁹Grad, H., *Proc. Symposium in Applied Mathematics*, Vol. XVIII, Amer. Math. Soc. (1967), p. 162.
- ²⁰L.S. Hall and T.C. Simonen, *Phys. Fluids*, **17**, 1014 (1974).
- ²¹Thompson, W.B., *An Introduction to Plasma Physics*, Pergamon, 1962.
- ²²H.L. Berk, Y.Z. Zhang, *Phys. Fluids* **30**, 1123 (1987).
- ²³S. Hiroe, private communication, (1987).

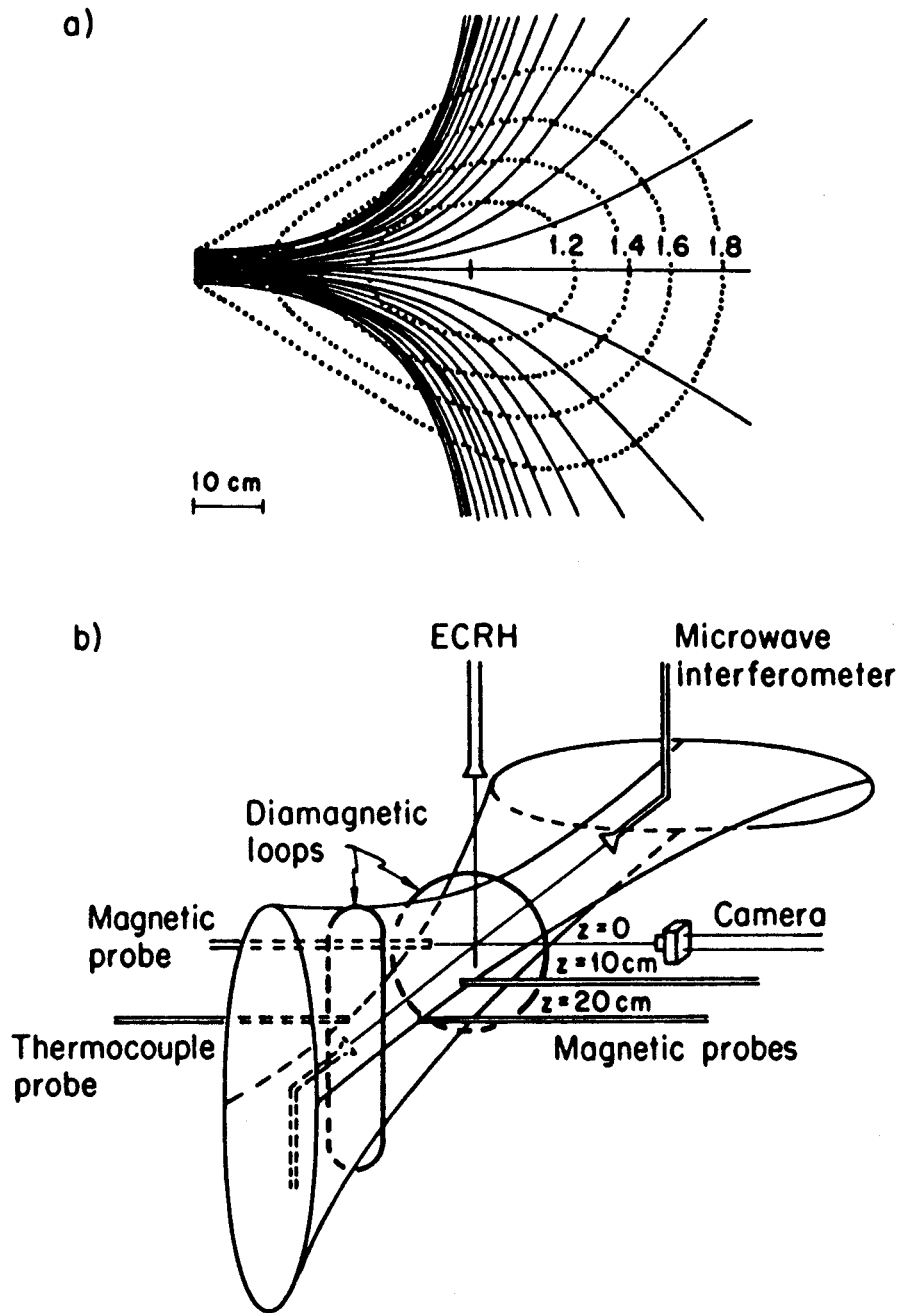


FIG. 1. (a) Constancy B magnetic field geometry. The solid lines are field lines and the dotted lines are surfaces of constant magnetic field. The values on the magnetic field contours are the mirror ratios with respect to the field at the center of the magnetic well. (b) Experimental setup for the equilibrium study. The origin of the (x,y,z) coordinate system is at the midplane.

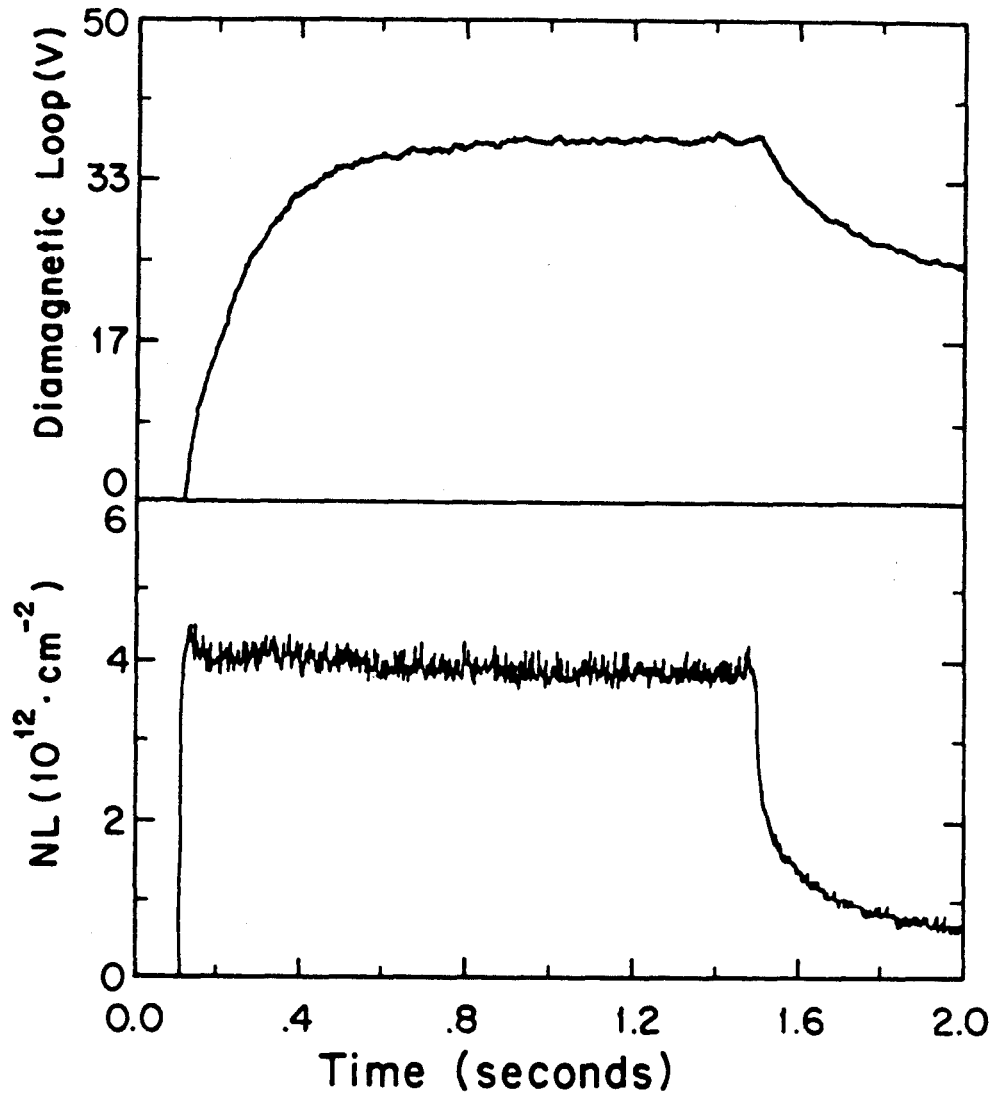


FIG. 2. Time history of plasma diamagnetism and line integrated density. The ECRH is on between 0.1 to 1.5 seconds. The conversion factor from the diamagnetic loop voltage to the peak beta is 1 Volt per 0.9 % beta according to the best fit pressure model.

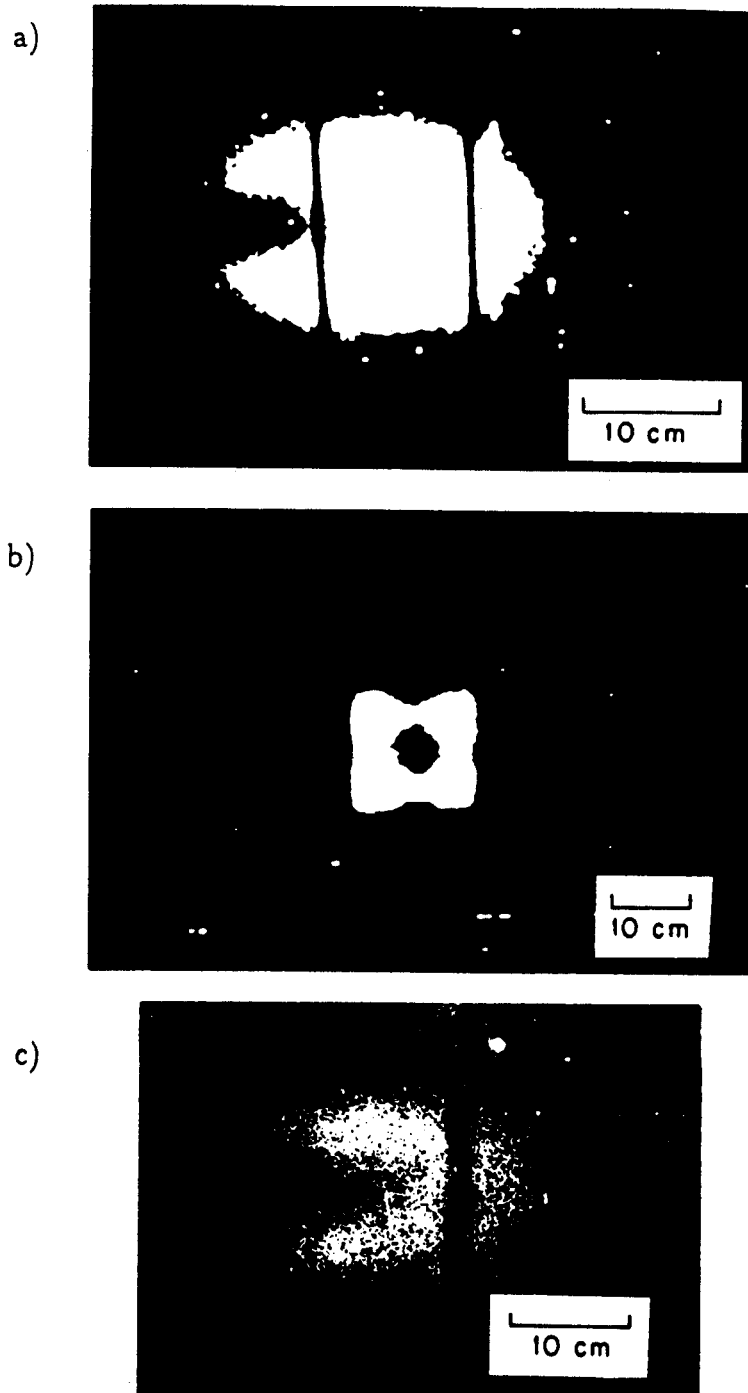


FIG. 3. Visible light and x-ray pinhole photographs of the plasma. (a) Visible light side view. (b) Visible light end view. The vertical bars are an ICRH antenna centered on the midplane. Both of the visible light images are taken 60 ms after ECRH turn-off. (c) X-ray pinhole picture obtained with direct exposure method. The dark bar is the shadow of the diamagnetic loop.

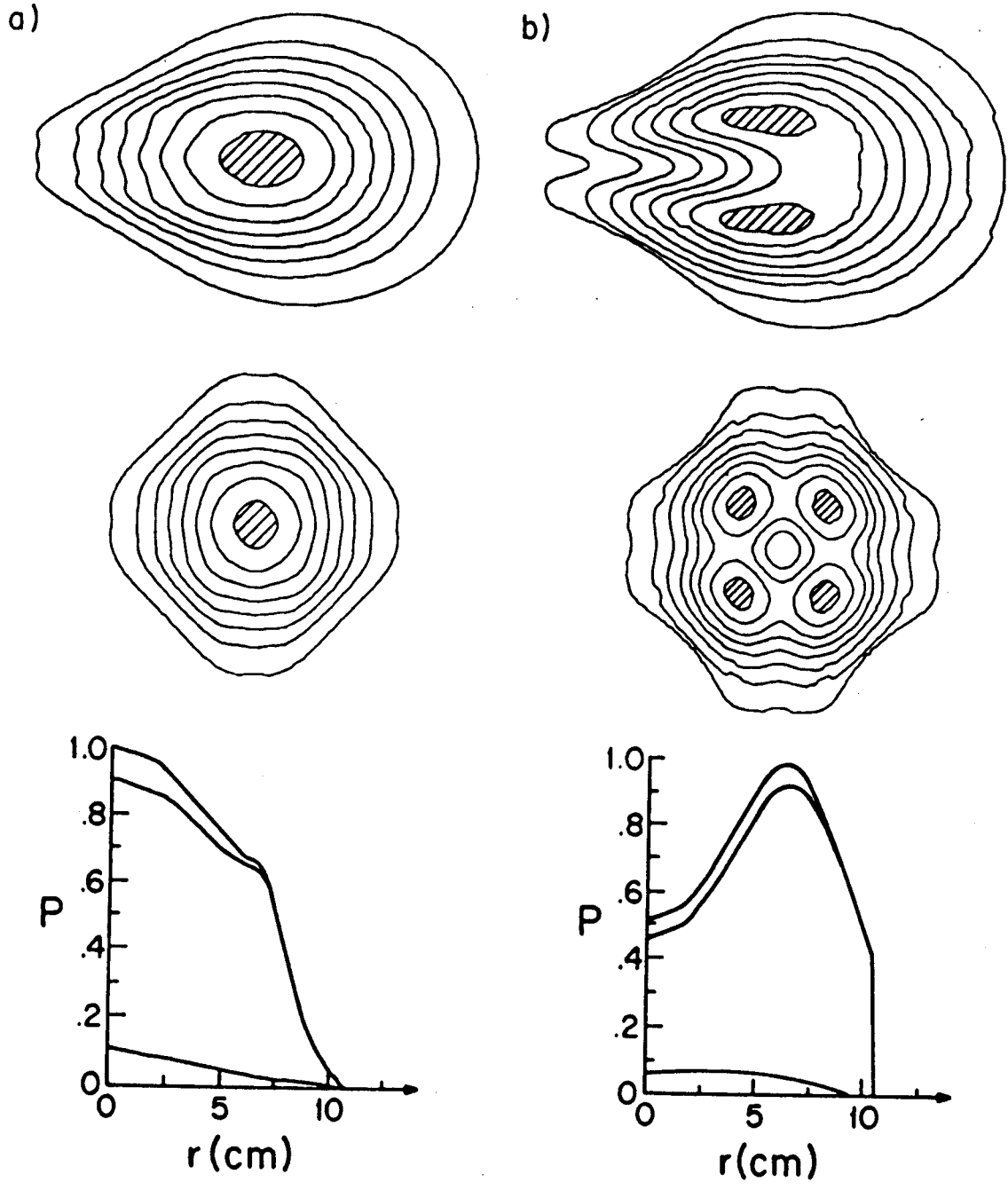


FIG. 4. Line integrated model plasma pressure profiles. (a) A radially peaked profile. (b) A 50 percent hollow profile. The highest contours are shaded. The radial pressure profiles $P_{||}$ (lowest curve), P_{\perp} , and P_{tot} (higher curve) are plotted as function of radius along the 45° line at the midplane.

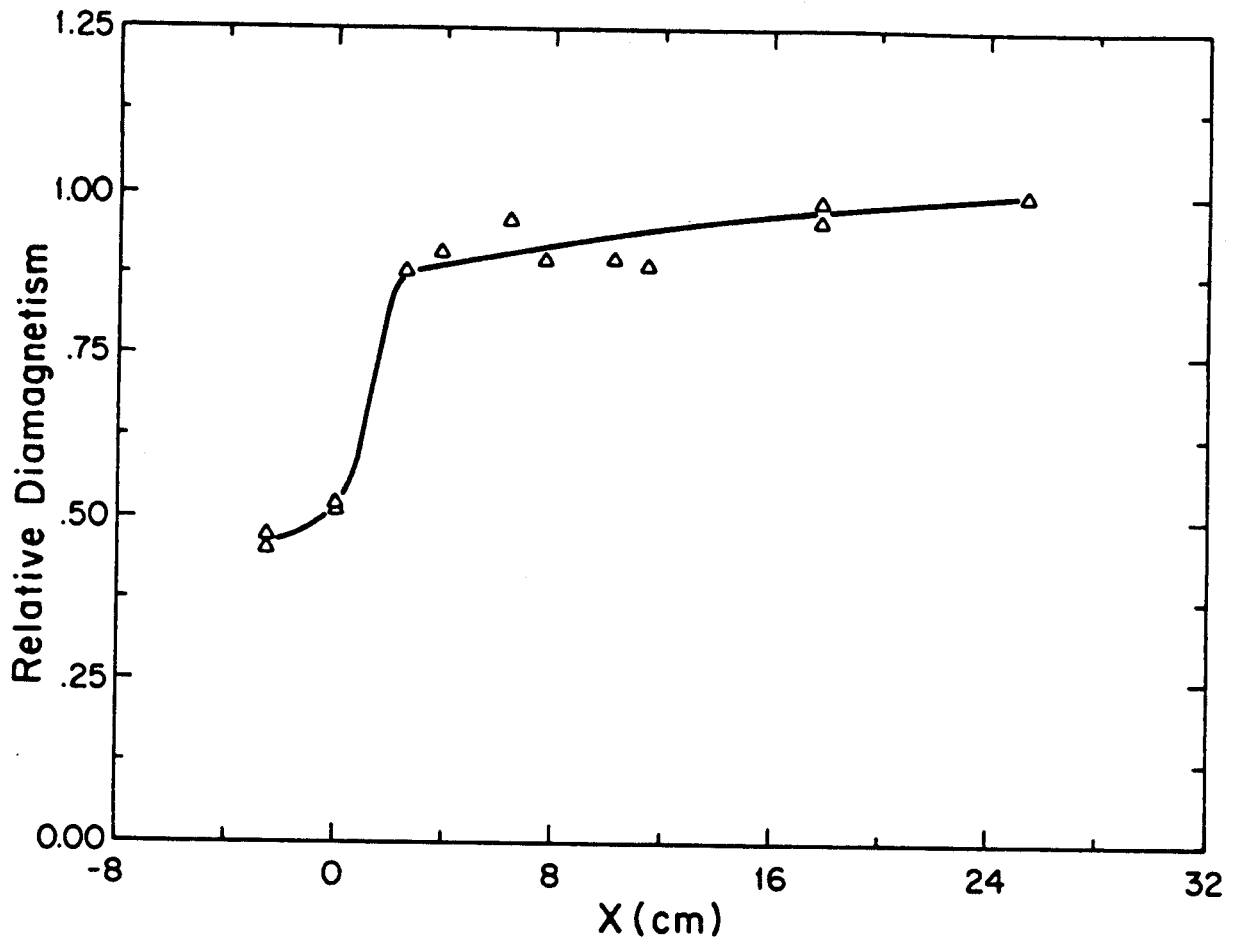


FIG. 5. Relative diamagnetic signal measured during a skimmer probe radial scan in the horizontal symmetry plane at $z = -10$ cm (see Fig. 1b.). The solid line is a visual fit of the data points.

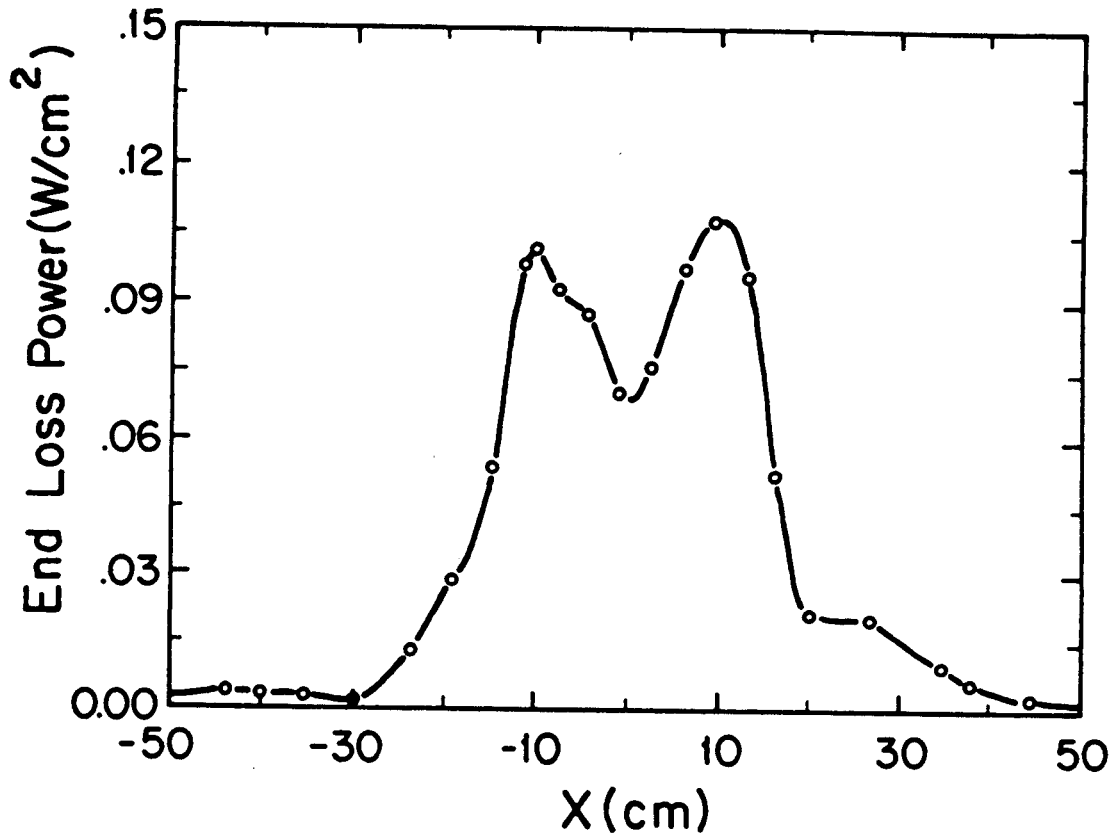
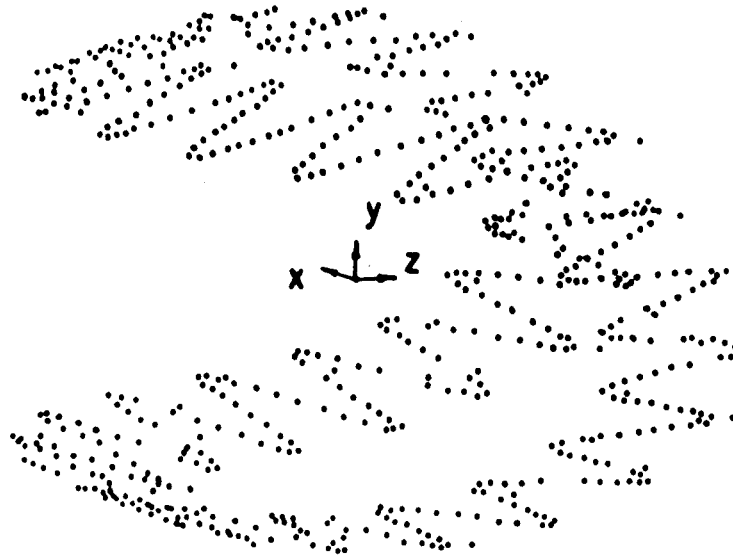


FIG. 6. End loss power distribution measured with a scintillator probe in the horizontal symmetry plane outside the mirror peak. The radial position is mapped to the midplane.

a)



b)

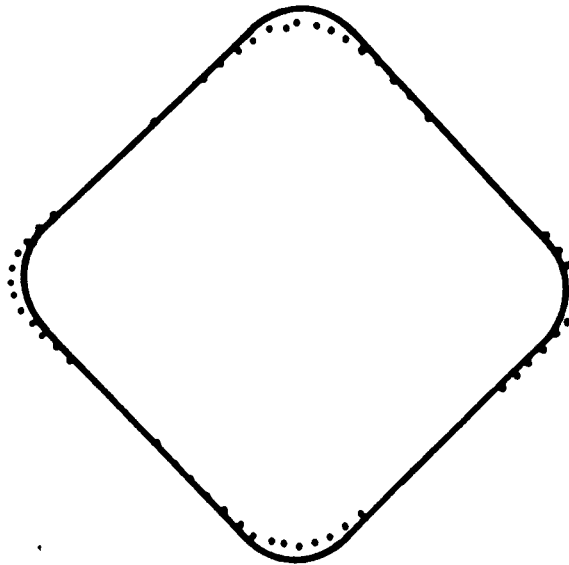


FIG. 7. Calculated drift orbit of a 360 keV electron in the vacuum magnetic field. (a) Guiding center trajectory. (b) Drift surface. The drift surface is obtained by mapping the guiding center positions along flux lines back to the midplane.

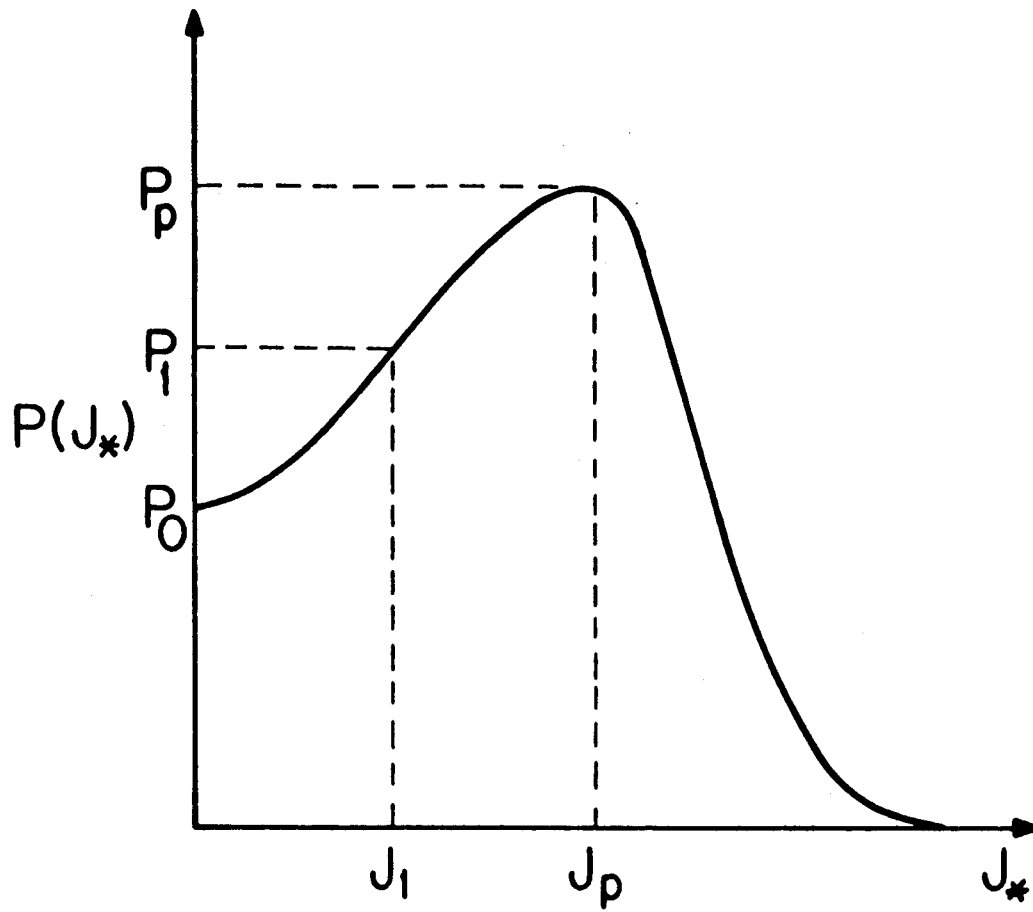


FIG. 8. Radial pressure profile model.

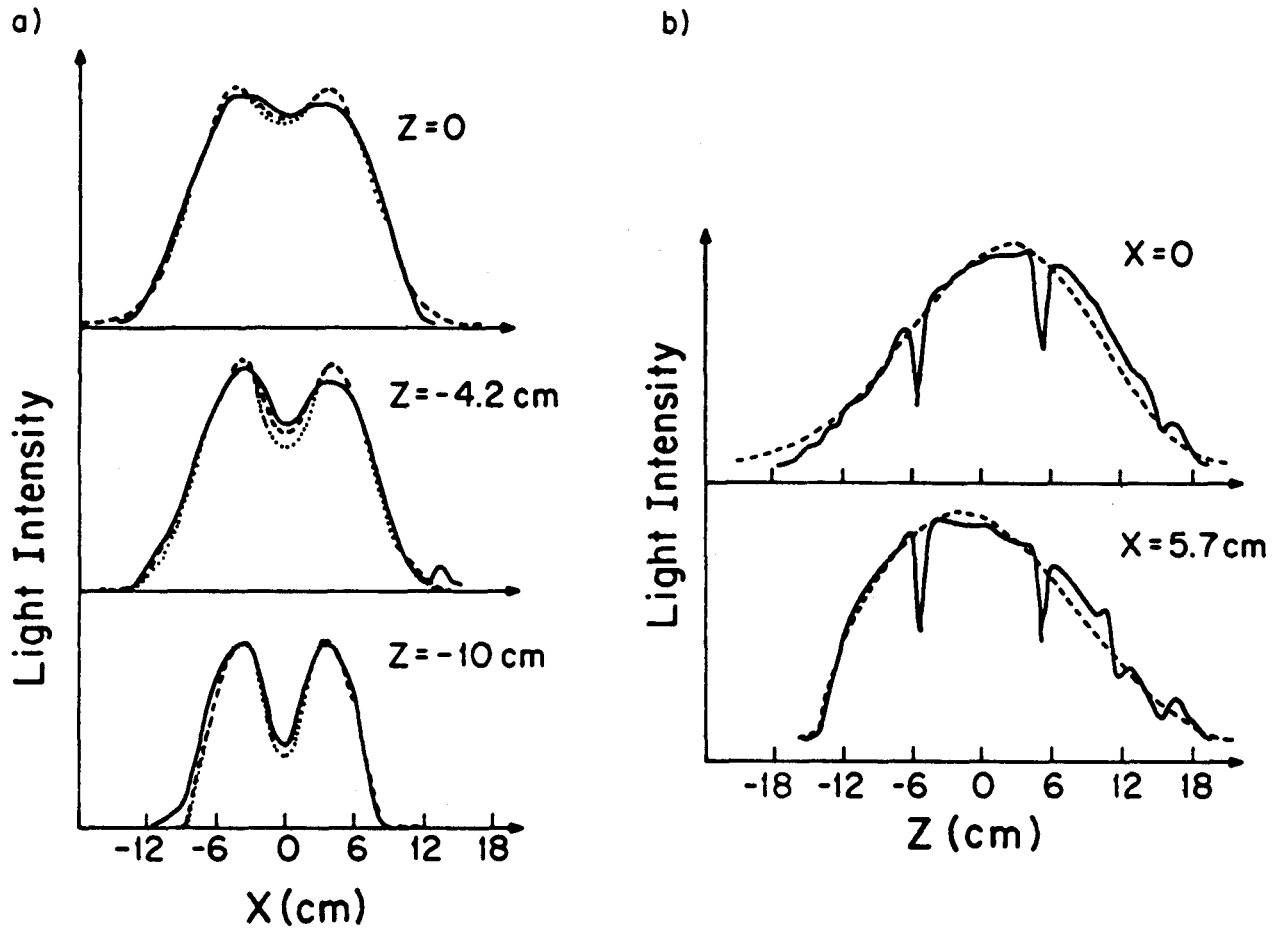


FIG. 9. Comparison between the measured and the simulated visible light intensity traces. (a) Radial light intensity traces at three axial locations. (b) Intensity traces parallel to the axis. The solid lines are the light intensity traces measured from the visible light photograph shown in Fig. 3a. The dashed lines are the simulations using a 50 % hollow plasma density profile. The dotted lines are the simulations from a 60 % hollow profile to show the sensitivity of the analysis to the hollowness parameter.

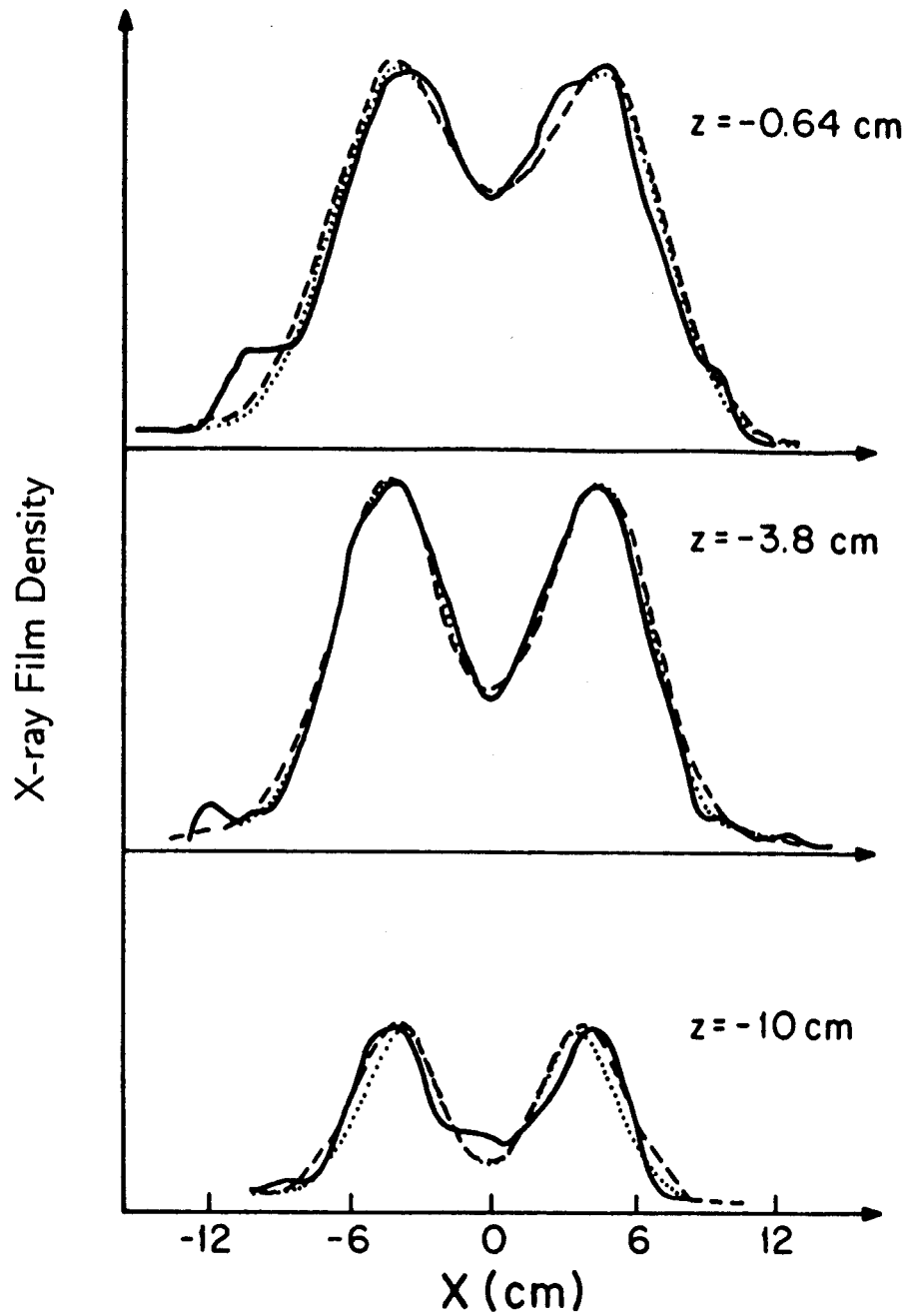


FIG. 10. Comparison between the measured and the calculated x-ray intensity traces. The solid lines are the density traces measured from the x-ray film. The dashed and the dotted lines are from the best fit profiles for the n_{eh}^2 and the $n_{eh}^{3/2}$ models.

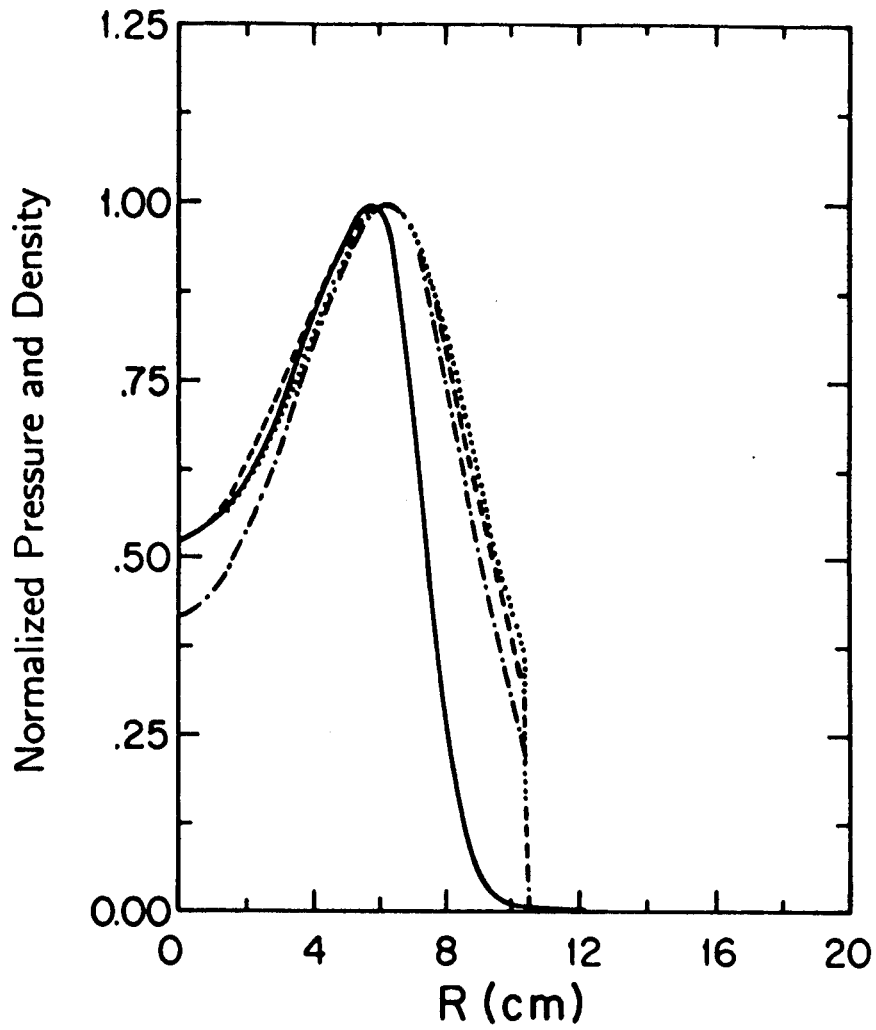


FIG. 11. The best fit radial plasma density and pressure profiles at 45 degrees at the midplane. The dotted, dashed and dash-dot lines are the hot electron density profiles determined from the visible light image, the x-ray image with the n_{ch}^2 model and the x-ray image with the $n_{ch}^{3/2}$ model, respectively. The solid line is the pressure profile determined from the magnetic measurement, with the hollowness set according to the hot electron density profile.

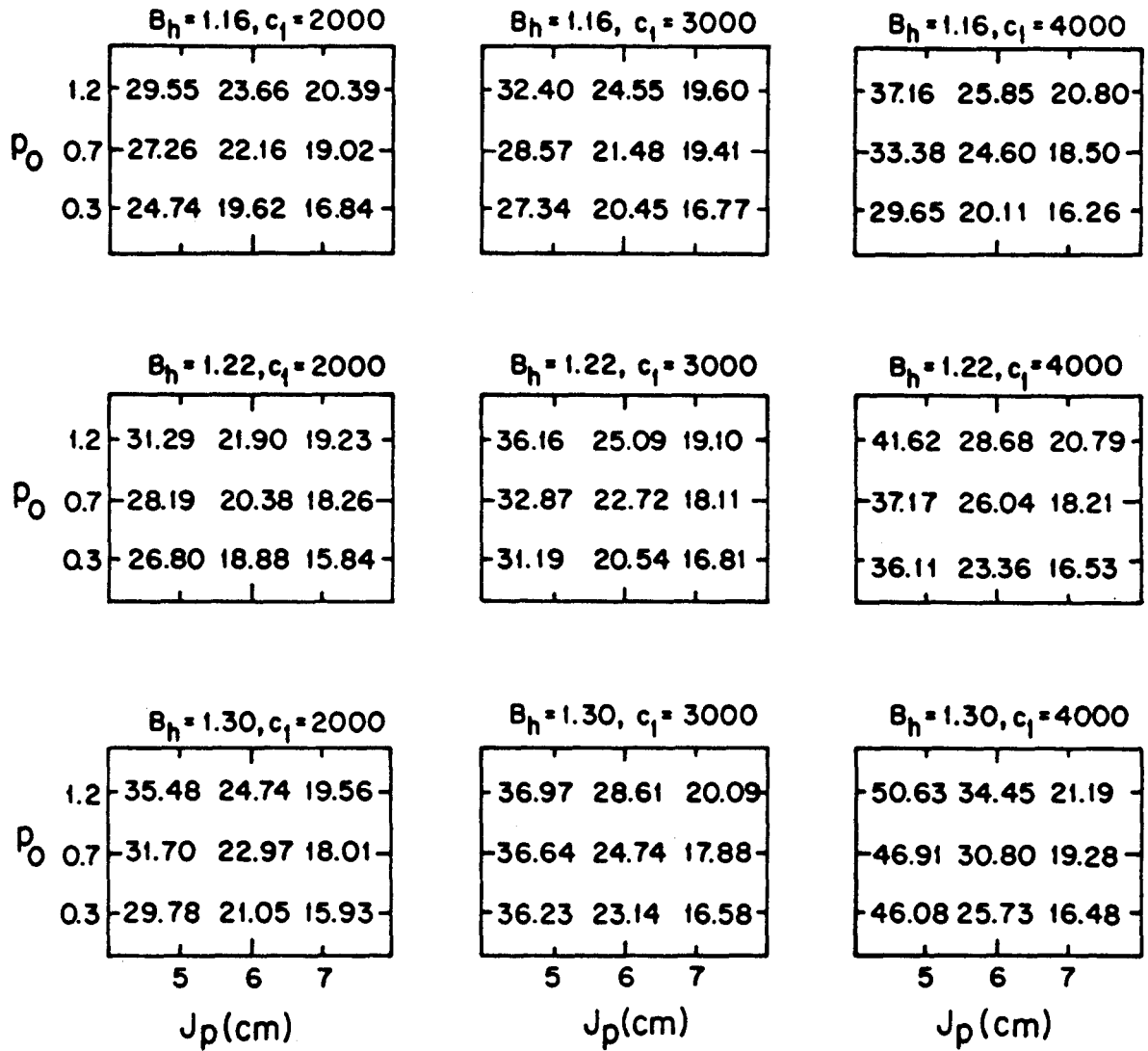
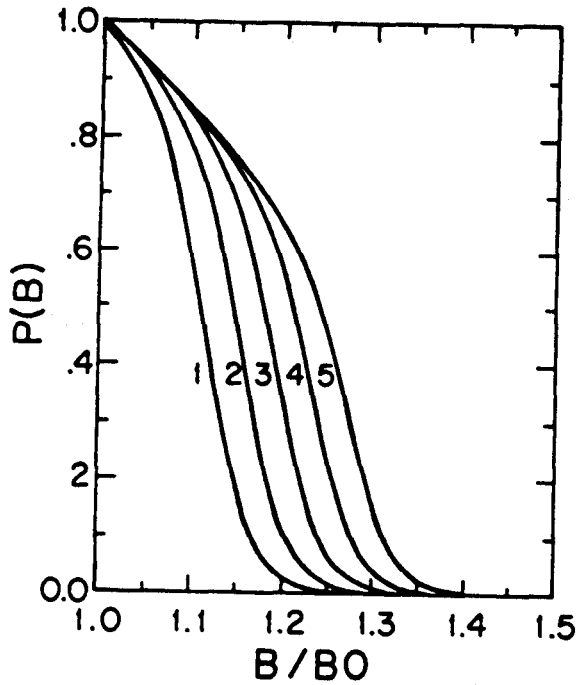
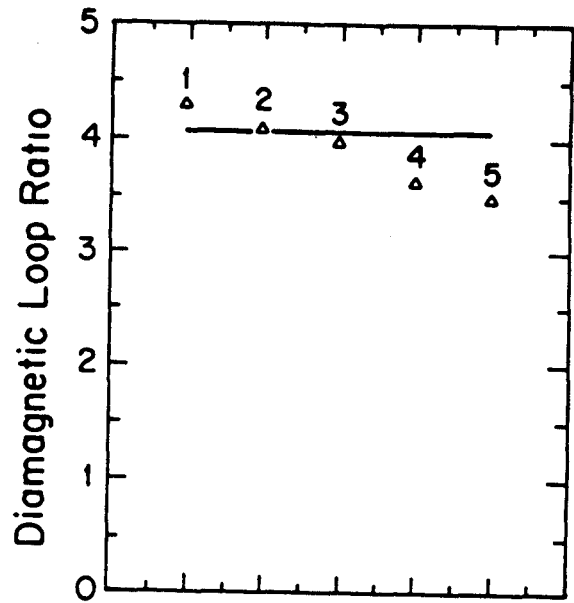


FIG. 12. Calculated signal ratios between the midplane diamagnetic loop and a B_z probe at $x=15.2$ cm on the midplane. The measured signal ratio is 22.5 ± 1 . The calculated results from 81 model pressure profiles are presented in the nine 3×3 matrices so that four dimensional profile parameter variations can be analyzed simultaneously.



(a)



(b)

FIG. 13. Calculated signal ratios between the midplane diamagnetic loop and an elliptical diamagnetic loop located at $z=22$ cm from 5 model axial pressure profiles. (a) Pressure profiles. (b) Calculated signal ratios. The measured signal ratio is 4.05 ± 0.1 , which is shown by the solid line.

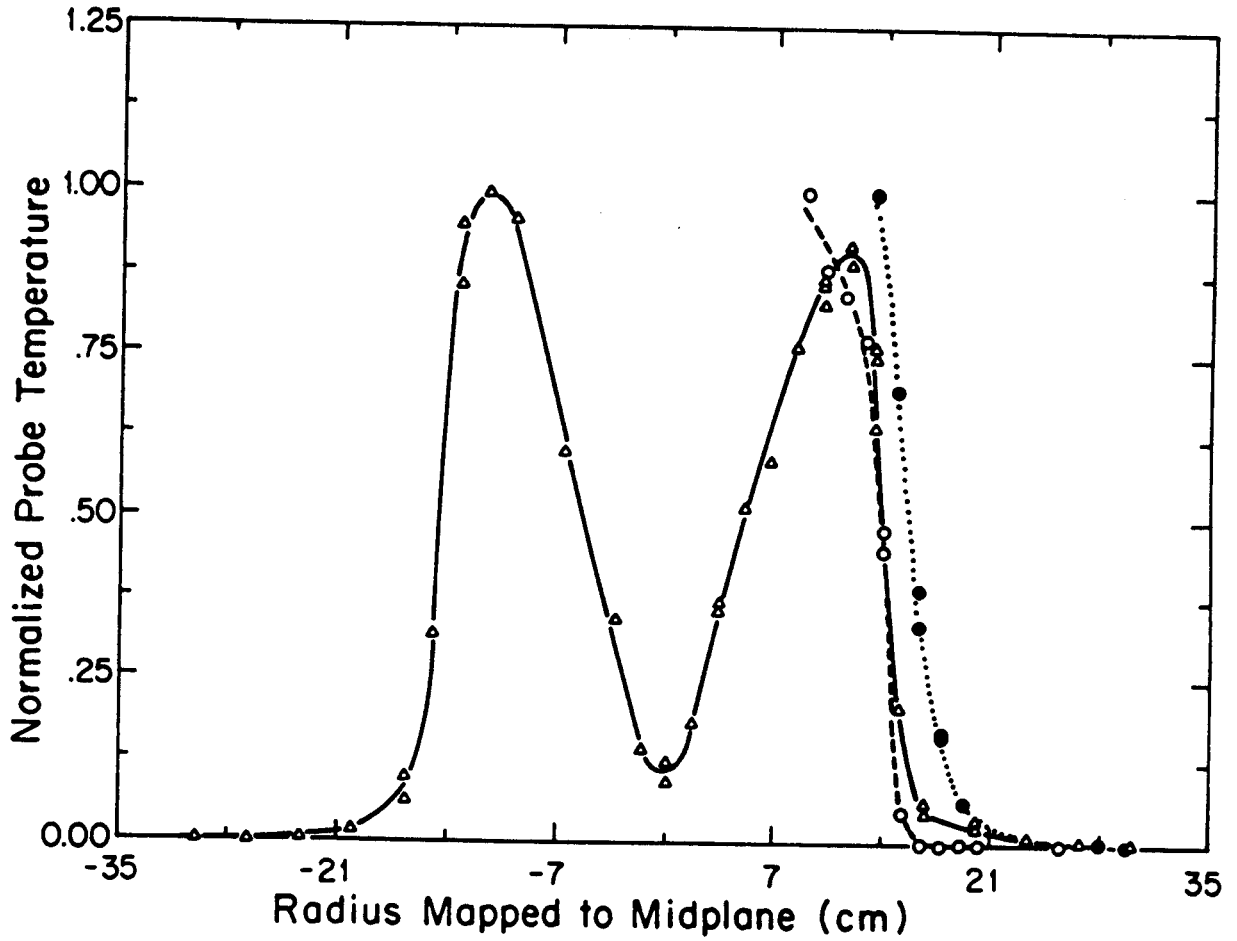


FIG. 14. Thermocouple temperature profile measured at three axial locations. The radial positions are mapped to the midplane. The dashed, dotted and solid lines connect the data points measured at $z = 0, 10,$ and 20 cm, respectively. The peak temperature at each axial location is normalized to 1. The midplane radius of the field line tangent to the ECRH resonant surface is 19 cm.

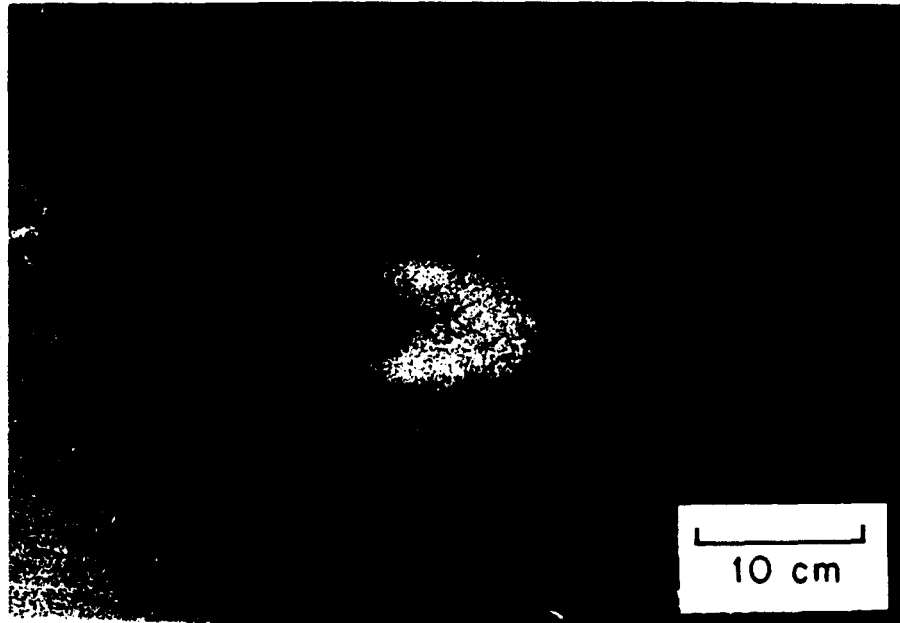


FIG. 15. X-ray pinhole photograph taken during a $B_0=3.6$ kG shot. The structure of the plasma profile is the same as measured in $B_0=3$ kG shots. The plasma radius is nearly 1 cm (or 25 %) larger than the ECRH resonance surface and the expansion is associated with the increase of the total diamagnetism.

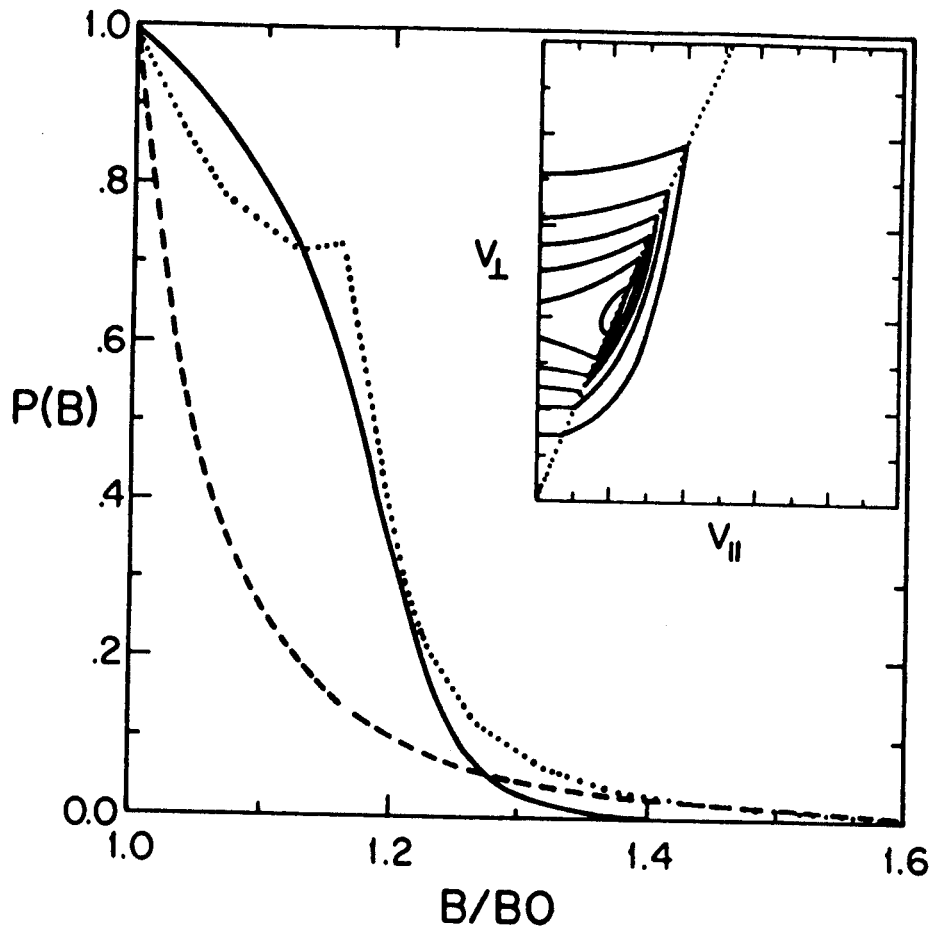


FIG. 16. $P(B)$ profile determined from the magnetic measurement compared with the pressures calculated from two velocity space distribution functions. The dashed line is the pressure from a bi-Maxwellian loss cone distribution with $T_{\perp}/T_{\parallel} = 5$. The dotted line is the pressure from the ECRH loss cone distribution shown in the inset.

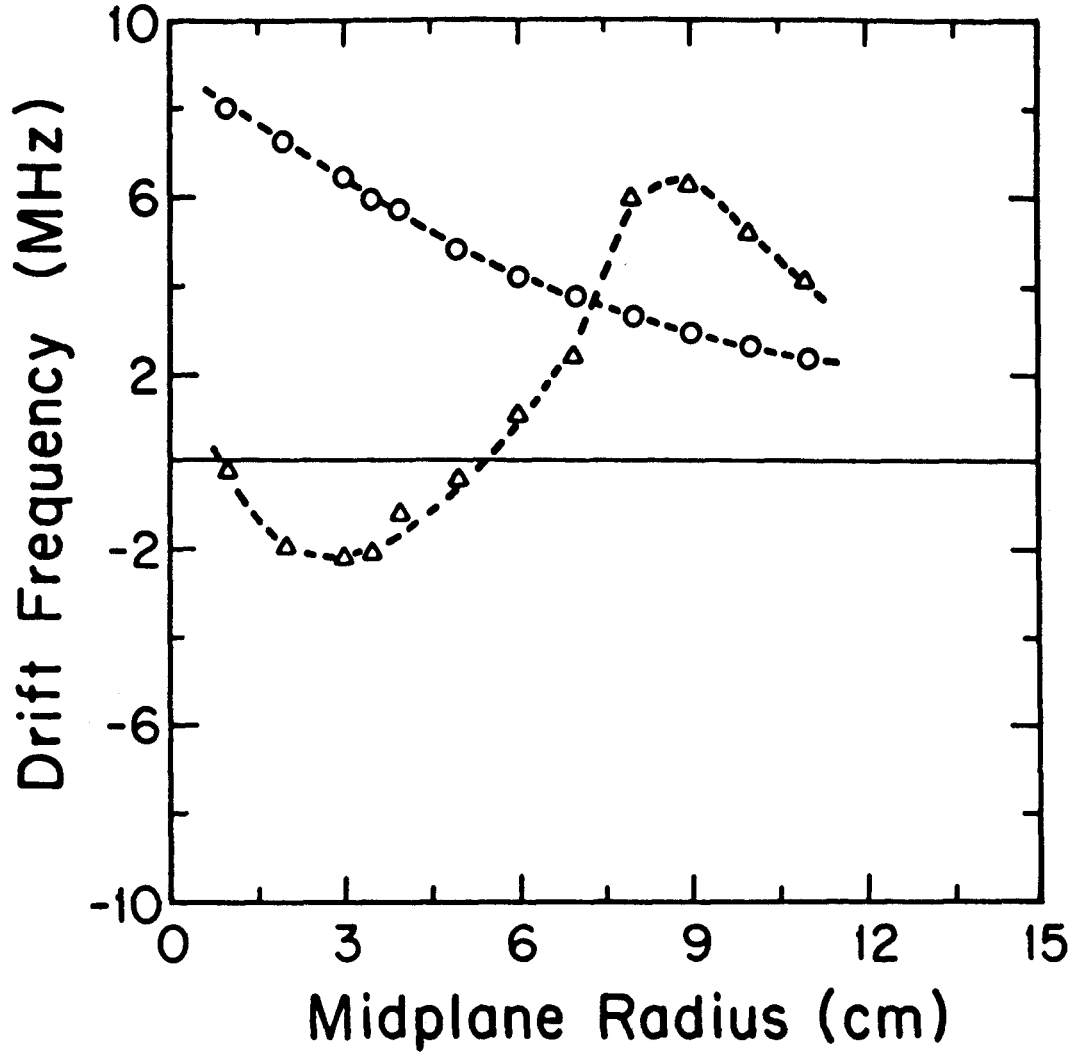


FIG. 17. The calculated bounce averaged drift frequency of a 350 keV electron in the 30 percent beta equilibrium magnetic field. The circle points and the triangle points are calculated using the vacuum magnetic field and the finite beta modified field, respectively. The negative value indicates that the direction of the drift is reversed. The radius is along the x-axis in the horizontal symmetry plane.